SORTING OF BIOLOGICAL CELLS IN A MICROFLUIDIC CHANNEL USING HOLOGRAPHIC OPTICAL TWEEZERS COMBINED WITH RAMAN SPECTROSCOPY

Ph.D. THESIS

Uğur PARLATAN

Department of Physics Engineering

Physics Engineering Programme

JANUARY 2017

ISTANBUL TECHNICAL UNIVERSITY ★ GRADUATE SCHOOL OF SCIENCE ENGINEERING AND TECHNOLOGY

SORTING OF BIOLOGICAL CELLS IN A MICROFLUIDIC CHANNEL USING HOLOGRAPHIC OPTICAL TWEEZERS COMBINED WITH RAMAN SPECTROSCOPY

Ph.D. THESIS

Uğur PARLATAN
(509102127)

Department of Physics Engineering

Physics Engineering Programme

Thesis Advisor: Prof. Dr. Günay BAŞAR

JANUARY 2017

İSTANBUL TEKNİK ÜNİVERSİTESİ ★ FEN BİLİMLERİ ENSTİTÜSÜ

SORTING OF BIOLOGICAL CELLS IN A MICROFLUIDIC CHANNEL USING HOLOGRAPHIC OPTICAL TWEEZERS COMBINED WITH RAMAN SPECTROSCOPY

DOKTORA TEZİ

Uğur PARLATAN
(509102127)

Fizik Mühendisliği Anabilim Dalı

Fizik Mühendisliği Programı

Tez Danışmanı: Prof. Dr. Günay BAŞAR

OCAK 2017

Uğur PARLATAN, a Ph.D. student of İTU Graduate School of Science Engineering and Technology student ID 509102127, successfully defended the thesis entitled "Sorting Of Biological Cells In A Microfluidic Channel Using Holographic Optical Tweezers Combined With Raman Spectroscopy", which he prepared after fulfilling the requirements specified in the associated legislations, before the jury whose signatures are below.

Thesis Advisor :	**Prof. Dr. Günay BAŞAR** ISTANBUL Technical University	....
Jury Members :	**Doç. Dr. İpek Kanat ÖZTÜRK** ISTANBUL University	....
	Yrd. Doç. Dr. Alexander JONAS ISTANBUL Technical University	....
	Doç. Dr. Baki ALTUNCEVAHİR ISTANBUL Technical University	....
	Prof. Dr. Alper KİRAZ KOÇ University	....

Date of Submission : 02 January 2017
Date of Defense   : 31 January 2017

To my mother, my spouse and children,

FOREWORD

After a very busy and stressful, however entertaining period of six years, the thesis has ended. I have learned a lot, both about the scientific part of my thesis and the methods of coping with a project. I would like to reflect on the people who were there for me and supported and during this period.

First, I want to thank Günay Başar for his patience in directing my thesis work, his support for increasing the quality of this work, and his efforts to find resources for the study. I am also grateful to Prof. Dr. Gönül Başar for her intellectual and logistic support for my thesis. I would like to express my sincere gratitude to the thesis juries, for their valuable ideas contributing to the thesis process.

I would like to thank Assoc. Prof. Dr. Ercan Baştu, for him to help us improve our understanding in medical field via the collaboration we were in. I thank Doğukan Bingöl and Merve Sirkeci, for their help during the experiments in Istanbul University.

I am grateful to the ITU BAP unit for their financial support for the thesis work and the research project.

I thank every loving family member who has tolerated me during the most intense times of my study.

January 2017   Uğur PARLATAN

x

TABLE OF CONTENTS

ABBREVIATIONS

HOT   **:** Holographic Optical Tweezers
SLM   **:** Spatial Light Modulator
PS   **:** Polystyrene
GUI   **:** Graphical User Interface
FRET   **:** Fluorescence Resonance Energy Transfer
SERS   **:** Surface Enhanced Raman Spectroscopy
GSW   **:** Weighted Gerchberg-Saxton
PCA   **:** Principal Component Analysis
CCD   **:** Charge Coupled Device
LDA   **:** Linear Discriminant Analysis
NA   **:** Numerical Aperture
LCoS   **:** Liquid Crystal Layer On Silicon
TN   **:** Twisted Nematic
DVI   **:** Digital Visual Interface
VGA   **:** Video Graphics Array
AOM   **:** Acousto-Optic Modulator
DOE   **:** Diffractive Optical Elements
CGH   **:** Computer-Generated Holograms
TN   **:** Twisted Nematic
BFP   **:** Back Focal Plane
CPU   **:** Central Processing Unit
KHD   **:** Kramers Heisenberg Dirac
MEMS   **:** Microelectromechanical Systems
PDMS   **:** Polydimethylsiloxane
PMMA   **:** Polymethylmethacrylate
SNR   **:** Signal To Noise Ratio
SVD   **:** Singular Value Decomposition
USB   **:** Universal Serial Bus
MT   **:** Multi – Track
REF   **:** Raman Edge Filter
HORT   **:** Holographic Optical Raman Tweezers
IPA   **:** Isopropyl Alcohol
UV   **:** Ultraviolet
FVB   **:** Full Vertical Binning
MO   **:** Microscope Objective
PBS   **:** Phosphate Buffer Saline

SYMBOLS

F	: Force
n	: Refractive Index
P	: Power
c	: Speed of light
σ	: Cross section (2.3), standard deviation (2.29)
t	: Time
α	: Dimensionless size parameter (in 2.3); divergence angle from the lens (2.12), polarizability (2.58)
m	: Effective refractive index
r	: Radius of the particle (in 2.3), reflection angle (in 2.10), position vector (in 2.19), distance of particles to equilibrium points (2.40)
E, U	: Radiation field vector
I	: Field intensity
R	: Reflection coefficient
T	: Transmission coefficient
θ	: Angular deviation between incident light and the sphere normal, vibronic wave function (in 2.66)
φ	: Phase
d	: Thickness of the material that the light travels in
f	: Focal length of the lens
a	: Pixel pitch
λ	: Wavelength of the light, electronic wavefunction (in 2.66)
τ	: Switching time for the liquid crystal
(x,y,z) (u,v,w)	: Spatial coordinates
k	: Wavenumber
e	: Efficiency
u	: Uniformity
ν	: Frequency of light
m	: Mass
μ	: Effective mass, induced dipole (in 2.65)
w	: Radial frequency
q	: Effective distance
E	: Total energy
T	: Kinetic energy
V	: Potential energy
h	: Planck's constant
$\mathbf{D_e}$	: Dissociation energy
β	: A coefficient for the curvature of the potential well
$\mathbf{\chi_e\omega_e}$	: Magnitude of anharmonicity
g	: Degeneracy of the states
F	: Orthonormal vector
Σ	: Covariance matrix

LIST OF TABLES

LIST OF FIGURES

SORTING OF BIOLOGICAL CELLS IN A MICROFLUIDIC CHANNEL USING HOLOGRAPHIC OPTICAL TWEEZERS COMBINED WITH RAMAN SPECTROSCOPY

SUMMARY

Investigation of single cells is crucial, since the measurement from population gives an average value that does not necessarily represent every individual in the population. Besides, sorting and sometimes counting the desired kind of cell is a measure of how the concentration of that cell. These types of micro-scale measurements are sometimes necessary, for example, to monitor the cell cycle, cell-signaling processes.

Serving to these purposes, first a holographic optical tweezers (HOT) setup was constructed. This setup was built by improving the current optical tweezers setup in the Laser Spectroscopy Laboratory in Istanbul Technical University. A brand new Holoeye Spatial Light Modulator (SLM) was installed in the system after it was calibrated using an interferometric setup. The holograms were calculated using a Gratings and Lenses algorithm written in MATLAB and implemented by the homemade GUI that manages all the tasks needed for trapping and spectroscopy.

The test particles to characterize the HOT setup were polystyrene (PS) particles. An array of four trapped PS particles was manipulated to the Raman spectrum measurement region by the software. The software communicates with the spectrometer and obtains multi-track spectra from the array that gives individual Raman spectra of each particle. These spectra identified by the software using the correlation coefficient of this measurement with the dataset that has already been prepared using PS particles and yeast cells.

The test Raman measurements of biological cells using yeast cells and E.coli cells were made to investigate the signal level in low exposure times. The measurement showed that, our system would not respond enough signal to classify particles when the sample is E.coli and the exposure time is one second. However, the yeast cells responded better in short exposure time. Considering these, the sorting test experiments were made using yeast cells and PS particles.

In a mixed solution of PS particles and yeast cells, an array of four particles whose members are randomly chosen was moved to the measurement region. According to the measurement and the following classification, the particles are targeted to the previously defined positions in the measurement cell. In these experiments, classifications were made with success.

A study to determine the embryo quality by Raman spectroscopy was made in collaboration with Istanbul University Medical School. In this study, it was aimed to find an objective method to assess embryo viability. The preliminary results showed that the sensitivity and specificity of these measurements are %93 and %77, respectively. A Mann-Whitney U test was applied on the band areas and all band area ratios obtained by band component analysis. The most significant one was found to be the band area ratio of 903/942 cm^{-1}. Comparing the measurements of amino acids

samples, it was determined that glutamine, glycine, proline, and valine has the most intense bands in the region that includes these significant bands. Among these, glutamine and glycine are the amino acids that contribute to embryo development most, according to the literature.

RAMAN SPEKTROSKOPİ VE HOLOGRAFİK OPTİK CIMBIZLAMANIN BİRLİKTE KULLANIMI İLE MİKROAKIŞKAN KANAL İÇERİSİNDEKİ BİYOLOJİK HÜCRELERİN AYRIŞTIRILMASI

ÖZET

Tek hücrelerin araştırılması hayati önem taşır çünkü nüfustan gelen ölçüm, nüfusta her bireyi temsil etmeyen ortalama bir değer verir. Ayrıca, arzu edilen hücre tipinin sıralanması ve bazen sayılması, o hücrenin derişiminin bir ölçüsüdür. Bu tür mikro ölçekli ölçümler bazen, örneğin hücre döngüsü, hücre sinyalleşme süreçlerini izlemek için gereklidir.

Bu sebeple, önce bir holografik optik cımbızlama seti (HOT) kurulumu yapılmıştır. Bu kurulum, İstanbul Teknik Üniversitesi Lazer Spektroskopi Laboratuvarı'nda mevcut optik cımbızlama setinin genişletilmesi ile kurulmuş ve ilerleyen ölçümler için İstanbul Üniversitesi Lazer Spektroskopi Laboratuvarı'nda yeniden bir set kurularak ölçümler alınmıştır.

Araştırma projesi kapsamında (İTÜ BAP – proje no 37851) satın alınan Holoeye Pluto BB marka SLM, bir çift yarık girişimi interferometrik düzeneği kullanılarak kalibre edildi. SLM ekranının bir tarafı siyah tutulup, diğer tarafında grilik seviyeleri 0-255 arasındaki değerlerle değiştirilerek faz ölçümleri yapıldı. Üretilen faz farkı – grilik seviyesi eğrisi lineer olana kadar gerilim seviyeleri değiştirildi. Son olarak gama düzeltmesi yapılarak kalibrasyon tamamlandı. Kalibre edilmiş SLM, daha sonra HOT sistemine yerleştirilerek 4-f düzeneği kuruldu.

HOT ve spektroskopi ile ilgili tüm görevleri gerçekleştirmek üzere bir Graphical User Interface (GUI) MATLAB'da tasarlanmış ve programlanmıştır. Hologramlar, *Gratings and Lenses* algoritması kullanılarak, HOT programı yardımı ile hesaplandı. HOT programı, girdi olarak örnek düzlemindeki parçacıkların olması istenen konumunu alır. Deney düzeneğimizde kullanılan kamera doğrudan yazılım ile ilişki kuramadığından, yazılım üzerinde kamera ile aynı çözünürlükte oluşturulan ekran ile kameradaki hareketler eşlenerek uzamsal kalibrasyon yapıldı. Bu sayede yazılım üzerindeki çerçeve üzerinden örnek düzlemindeki konumlar elde edilebildi. HOT deneylerinde kullanılan algoritmalar polistiren (PS) test parçacıkları ile test edildi.

HOT yazılımı tarafından oluşturulan dört adet spot örnek düzleminde test parçacıklarının tuzaklanması için kullanıldı. Dört tuzaktan oluşan bu PS parçacığı dizisi, yazılım tarafından Raman spektrum ölçüm bölgesine yönlendirildi. Yazılım, spektrometre ile iletişim kurduktan sonra bir saniye süre ile tek bir spektrum alır. Bu spektrum, CCD pikselleri y-ekseninde bölünerek her bir dilimden gelen sinyal ayrı ayrı ele alınacak şekilde işlendiği için (*multi-track*), her parçacığın bireysel Raman spektrumlarını elde bir seferde elde etmiş olur. Bu spektrumlar, PS parçacıkları ve maya hücreleri kullanılarak hazırlanmış olan veri kümesiyle karşılaştırılır. Bu karşılaştırmada kıstas ölçüm ile veri kümesi arasındaki korelasyon katsayısıdır. Önceden belirlenen eşik değerlere göre korelasyon katsayısının değeri sınıflandırma için gereken ölçütü belirler. Bu ölçüt kullanılarak parçacıklar her bir sınıf için atanan

bölgelere doğru yazılım tarafından ilerletilir. Başlangıç, ölçüm ve sınıflandırma sonrası son konumlar daha önceden belirlenmiş değerler olup, program bu değerleri kullanarak parçacıkları konumlandırır. Gidilecek konumlar daha önceden belirli olduğundan anlık hologram hesaplama yerine, önceden hesaplanmış hologramların kullanılması da tuzaklama ve ayrıştırma verimini oldukça artırmıştır.

Maya hücreleri ve E.coli hücreleri kullanılarak biyolojik hücrelerin test Raman ölçümleri düşük pozlama sürelerinde sinyal seviyelerini araştırmak için yapılmıştır. Örnek E.coli ve pozlama süresi bir saniye olduğunda parçacıkların sınıflandırılması için ölçüm sistemimizin yeterli sinyali vermediği görüldü. E.coli hücreleri ile sinyal elde edilebilmesi için eşik pozlama süresi değeri 30 saniye yeterli oldu. Bununla birlikte, maya hücreleri kısa pozlama sürelerinde daha iyi yanıt verdi. Maya hücreleri ile bir saniyelik ölçümlerde önemli bantları ortaya çıkmıştır. Korelasyon katsayının eşik değerinin ayarlanması ile mayalar için bir saniyelik ölçümler için ayrıştırma deneyinin mümkün olduğu görülmüştür. Bu göz önüne alındığında, sınıflandırma testi deneyleri maya hücreleri ve PS parçacıklar kullanılarak yapılmıştır.

PS parçacıkları ile maya hücrelerinden oluşan karışık bir çözeltide, sekizli spot dizisi dördü Raman spektrumları ölçüm bölgesinde, dördü de yazılım ekranın sol kenarında daha sonra ölçülmek üzere bekleyen tuzaklardır. İşlemin başlamasıyla birlikte ölçüm bölgesindeki tuzaklardan sinyal alınır. Ölçüm ve sonrasında yapılan sınıflandırmaya göre, parçacıklar ölçüm hücresinde daha önce tanımlanan konumlara yönlendirilir. Bu yönlendirme sırasında iki türlü parçacık iki farklı köşeye gider. İlk grup hareketini tamamladıktan sonra, ikinci grubun hareketine başlamasıyla birlikte ekranın sol tarafında bekleyen dörtlü grup ölçüm bölgesine doğru hareket eder. Bu döngü kullanıcı durdurana kadar devam eder. Bu deneylerde, sınıflandırma başarı ile yapıldı.

Raman spektroskopisi ile embriyo kalitesinin belirlenmesine yönelik bir çalışma İstanbul Üniversitesi Tıp Fakültesi'nden Dr. Ercan Baştu ile işbirliği içinde yapılmıştır. Bu çalışmada, embriyo canlılığını değerlendirmek için objektif bir yöntem bulunması amaçlanmıştır. Değerlendirme embriyoların yetiştiği atık kültür sıvılarından yapılmıştır. Hipotez, atık sıvısında en çok besin tüketen embriyonun en iyi gelişim göstereceği idi. Bu amaçla gönüllü kişilerden alınan örnekler ortalama 30 µL'lik hacimlerle İTÜ Lazer Spektroskopi laboratuvarına sıvı azot tankı içerisinde getirildi. Örnek hacmi küçük olduğundan, Raman hacmini büyütmek ve ölçümlerden en iyi sinyali alabilmek için disk şeklinde bir ölçüm hücresi üretildi. 16'sı hamilelik aşamasına geçemeyen, 15'i hamilelik aşamasına geçebilen 31 embriyo atık sıvısı örneğinden, 30 saniye pozlama zamanı ile arka arkaya 20 ölçüm, bu ölçüm hücresi içinde alınmıştır. Her atık sıvı ölçümünden önce saf su ölçümü ve sonrasında tolüen ölçümü alınmıştır. Tolüen ölçümü kalibrasyon aşamasında kullanılırken, saf su ölçümü, arka plan düzeltilmesi için kullanılmıştır. Ölçümler normalize edilmiş ve taban çizgileri üçüncü derece bir polinom taban profiline uydurularak çıkarılmıştır. Önişlem yapılmış spektrumlara bant bileşen analizi uygulanmış ve bu yöntem ile elde edilen bant alanlarına ve tüm bant oranlarına bir Mann-Whitney U testi uygulanmıştır. En önemlisi 903/942 cm^{-1} bant alanı oranı olarak bulunmuştur. Bu oranlara K-ortalama kümeleme analizi uygulanarak sınıflandırması yapılmıştır. Bu sınıflandırma sonucu, bu ölçümlerin duyarlılığı ve özgünlüğünün sırasıyla,% 93 ve% 77 olduğunu göstermiştir.

Bu çalışma içerisinde ayrıca fenilalanin, valin, glutamin, alanin, arjinin, tirozin, triptofan, glisin, prolin, serin, histidin, prolin, glutamat, ve sistein amino asitlerinin sulu çözeltilerinin Raman spektrumları ölçülmüştür. Bu ölçümler incelendiğinde,

glutamin, glisin ve prolin'in 903 cm^{-1} civarında ve valin'in 942 cm^{-1} civarında kendine ait en şiddetli bantlarının bulunduğu tespit edildi. Bunlar arasında, glutamin ve glisin literatüre göre embriyo gelişimine en çok katkı yapan amino asitlerdir. Bu sonuç en önemli bant oranının 903/942 cm^{-1} olduğu sonucumuzla uyum içerisindedir.

1. INTRODUCTION

Consider a solution of yeast cells and a PhD student desires to measure the hour-by-hour growth and nutrition relation. He/she measures the average growth of the cells every hour and compares it with the amount of the nutrition the population consumes. If the student tries to apply his result on an individual, how possibly will it match the conditions of the particular cell? Since the biological media are heterogeneous (cells are not identical, not in equilibrium, the biological parameters of the individuals are not same) the results will not match for many of the individual cells.

To overcome the difficulties discussed above, one can characterize each cell in a medium singly according to their physical properties and can separate the cells of interest from other kinds of particles. Among many separation techniques, it was hypothesized that sorting of single cells could non-invasively and effectively be achieved without using any labels using Holographic Optical Raman Tweezers (HORT). This method combines Raman spectroscopy and holographic optical tweezers. Holographic optical tweezers is a modified version of the optical tweezers method. In this method, micron sized particles can be immobilized and manipulated non-invasively by using the force components exerted by the light source.

Before the construction the holographic optical tweezers setup, the spatial light modulator (SLM) that needed to be added to the previous setup was calibrated. The calibrated SLM is placed to the new optical setup, which provides 4-f configuration. After the construction of the setup, realization of multiple traps was achieved. The software needed for HOT and calibration of the SLM was written on Matlab platform. Since the software can communicate with the spectrometer, too, the automation of the process could be achieved fully. This automation process included creating spots, moving particles to specific measurement position, measurement of Raman spectra of a 4-particle array, and movement of the particle to the related channels after identification.

During the PhD thesis, other than single cell sorting, medical studies using Raman spectroscopy were performed. This study aimed to show that one could assess the embryo quality with high sensitivity and specificity using optical methods without a need of a subjective comment. In the study, an unsupervised classification method on the Raman spectra of spent embryo cultures were applied to select the most viable embryo with the best percentage possible.

1.1 Purpose of Thesis

The purpose of this thesis is to achieve biological sorting using holographic optical tweezers setup. The sorting criterion was the Raman signal obtained from the cells, which gives a cell specific chemical signature from the sample of interest. After developing a software that controls particle manipulation, hologram calculation, communication with spectrometer, data pre-processing and identification, the experiments were supposed to be performed automatically.

1.2 Literature Review

Biological media are, generally, heterogeneous due to its nature. Physiological measurements on these media, therefore, give average result from the population. These measurements work well for many applications in the macroscopic scale. However, the individuals in the medium are neither identical nor in equilibrium. Their biochemical and physiological properties, such as grow rate, nutrient consumption are variable. Therefore, measurements on single cells give better results. This is well discussed in a review [1].

Microfluidics is a miniaturized flow control method that is highly practical for single cell studies. Microfluidic devices are fabricated using soft lithography. Soft lithography was first demonstrated by Xia and Whitesides [2]. These devices were combined with photonics and this is called optofluidics [3]. Microfluidics combined with spectroscopy and detection methods is a good recipe to reveal the biological mechanisms. Some of the physical methods combined with microfluidics are fluorescence spectroscopy [4], fluorescence resonance energy transfer (FRET) [5], Raman spectroscopy [6], surface enhanced Raman spectroscopy (SERS) [7], two photon spectroscopy [8], impedance spectroscopy [9].

There are several physical and chemical methods also found application in the field of separation and sorting of single cells most of which were well revised before [10-13]. Recently, Raman spectroscopy was used as a separator parameter in microfluidic applications [14-18]. This is a spectroscopic method discovered by Sir Chandrasekhar Venkata Raman in 1928 where the inelastic scattered photons from the molecules of the sample are collected using appropriate optics [19]. In his article, CV Raman explained his setup consists of sunlight as light source, a telescope (18 cm aperture and 230 cm focal length), a second lens (f = 5 cm) and his eyes as detectors. As the instrumentation improved, better results with spectroscopic design mercury light sources were obtained [20-23]. Eventually, after the invention of lasers, suitable laser sources for Raman spectroscopy such as Ar^+ (351.l-514.5 nm), Kr^+ (337.4-676.4 nm) and Nd:YAG (1064 nm) lasers were developed and laser Raman spectroscopy took place in literature with awaiting wide field of application [24]. Among these applications, Raman spectroscopy attracted great attention from the field of biology and medicine since water, which is the main component in biological media, has very low and broad contributions to spectra. The method does not need sampling in most of the applications, and is non-invasive when the right laser source is used. Some biomedical applications of Raman spectroscopy were reviewed by Lawson *et. al.* [25] and Choo *et. al.* [26]. Carey, also, explained the biochemical applications of Raman spectroscopy in his book together with the theoretical basis of the methods [27]. Başar *et. al.* used Raman spectroscopy to investigate pre-eclampsia disease the first time [28]. Parlatan *et. al.* found preliminary results to select the most viable embryo to improve IVF outcomes [29].

Among the optical techniques used in cell separation, optical tweezers is one of the label free methods. Particle trapping and manipulation, which is named "optical tweezers" is a phenomenon that is based on the fact that light can carry momentum and it can exert force on matter. Such effect relies on the physical phenomenon called radiation pressure, which was first suggested by Keppler who was studying comet tails. Maxwell published the foundations of "radiation pressure" in 1873 [30]. The first successful experiments that used arc lamps to move vanes, proved radiation pressure exists. Two independent studies were made in the same year, 1901. One was made by P. N. Lebedev who used extremely low gas pressures and the other one was made by E. F. Nichols and G. F. Hull who used high gas pressures with silvered vanes to ensure

the experiments are valid only under high pressure conditions [31, 32]. The latter group made the first quantitative study to prove Bartoli laws of radiation pressure [33].

Optical tweezers that is being used in the current form was invented by Arthur Ashkin. He used to work in Bell labs between 1970 and 1990 and had an interest in radiation pressure and manipulation of micron-sized particles. The first study to build the foundations of the optical trapping we currently use today was published in 1970 [34]. He hypothesized that one could obtain radiation pressure by avoiding radiometric forces (these forces can result in movement of particles by thermophoresis, photophoresis or diffusiophoresis) that stem from thermal effects using high laser intensity. He used micron sized spherical glass particles to avoid thermal effects and chose the diameters as big as the wavelength of the light shed on the particle ($d \cong \lambda$). The first realization of single beam optical traps was achieved in 1986 by Ashkin, Dziedzic, Bjorkholm and Chu [35]. They have clearly explained the forces acting on the particles in both Rayleigh regime ($d \ll \lambda$) and Mie regime ($d \gg \lambda$). Ashkin and colleagues made many research in the area optical trapping including atom trapping and manipulating microorganisms such as tobacco virus.

Trapping more than one particle has come out as an essential need for optical manipulation research in the micro scale, especially for the biological applications. In the first applications of the multiple trap, time sharing of a single beam was used to obtain multiple traps by rapidly changing the lateral position of the mirror in the Fourier plane (see figure 2.9) which results in a lateral position change in sample plane [36]. This method involved rapidly scanning of the intensity gradient along the desired position of the traps. This means, switching on and off the laser faster than the time needed for the particle to drift of the trap allows time-sharing of the intensity gradient of the laser. Alternative to mirrors, acousto-optic modulators (AOM) were used in multiple trapping setups to scan the beam faster [37, 38]. Use of diffractive optical elements (DOE) gave better results especially after the improvement of spatial light modulators (SLM) which are programmable pixelated devices. Duffresne *et. al.* proposed the first DOE adapted HOT setup that could trap a 4x4 dielectric sphere array [39]. After this early use of computer generated holograms for multiple trapping, this method was named as "*Holographic Optical Tweezers (HOT)*". Liesner *et. al.* was the first to show an optical tweezers setup that replaces a SLM instead of mirror could achieve both lateral and axial positioning [40]. Curtis *et. al.* made a break-through for

this method by demonstrating combination of many traps and modification of individual trap types [41]. The developed methods for creating computer generated holograms include gratings and lenses algorithm, Gerchberg – Saxton algorithm and random mask algorithm. When, where and how to use these algorithms have already been discussed by Spalding *et. al.* [42]. In this paper, the uniformity and the efficiency of these algorithms are also discussed. The Weighted Gerchberg-Saxton (GSW) algorithm is proved to be the most superior among these algorithms by means of uniformity and efficiency.

Combination of Raman spectroscopy and optical tweezers or HOT was demonstrated to be useful in microfluidic cell separation. Creely *et. al*. [43] studied floating living cells. They used the 1064 nm trapping beam to move the sample back and forth. Thus, the second 785 nm laser could scan the floating cell by illuminating different location of it. Creely et. al. [44], used the same strategy of Raman imaging to image neoplastic cells. Ramser et. al. [45] also combined Raman and optical tweezers together with microfluidics to study single red blood cells. Butler et. al. [46], characterize individual aerosol droplets using HOT and Raman spectroscopy. In this study, each trapped aerosol particle was moved to the region, which they called "Raman active region" to measure them individually. Kong and Chan [47] constructed a combination of Raman and HOT setup to obtain multifocal Raman signal acquisition from an array of polystyrene (PS) particles. In this study, Raman measurement of the particles in the array was achieved simultaneously. The spectrometer was modified to have five slits, which allowed collecting signal from five lateral positions. Resolution of superposed signal from the particles in the axial positions was made by a data processing algorithm they suggest. There is a study combines Raman spectroscopy and optical tweezers investigates living algae in a microfluidic channel to sort them according to their unsaturated lipid ratios [48].

Multivariate methods (especially PCA - Principal Component Analysis) are essential statistical methods to be used in spectral analysis today. Although PCA and spectroscopy were used back in 1950 [49], what makes PCA an indispensable tool for Raman spectral analysis is its power to reduce dimensionality and give a qualitative vison of classification using the scores plot. This technique (generally together with another classification methods) were used in identification of several diseases [50-54] and biological materials (cells, tissues, organisms, fluids) [55-58] using Raman

spectroscopy. The mathematical derivation of PCA was given in the original paper of Pearson in 1901 [59]. Hotelling's psychometrics study in 1933 [60] is accepted as the first original application of the PCA.

1.3 Hypothesis

This thesis aimed to separate trapped biological particles (isolated cells, living cells such as bacteria or yeast cells) using the Raman signal acquired from them real time. As seen in the literature section, a lot of sorting method for cell separation is present. In our study, it was planned to sort the biological cells in microfluidics channels using HOT and Raman spectroscopy. It is possible to create an array of multiple particles in the measurement region and to obtain Raman spectra of individual particles by binning the Charge Coupled Device (CCD) vertically. Although one can obtain weak spectral signal with Raman spectroscopy, it is possible to identify particles with low exposure times using multivariate statistical analysis methods such as principal component analysis (PCA) and linear discriminant analysis (LDA) of just calculating the correlation matrix of the individual measurement and the pre-calculated dataset.

2. THEORETICAL BACKGROUND

2.1 Optical Tweezers

Optical tweezers is a method to trap and manipulate micron size (sometimes nano size) particles by using a tightly focused beam. A high numerical aperture (e.g. NA=1.2) microscope objective can help provide this condition. This tightly focused beam applies two kinds of forces on the illuminated particle: Gradient force and scattering force. Scattering force stems from the beams that the trapped particle deflects. Gradient force took its name after the derivation of the lateral force component that is proportional to the gradient of the field. As mentioned above, comparing the size of the particle to the wavelength of the light, there are two kinds of regimes: Rayleigh regime (d≪λ) and Mie regime (d≫λ), where d is the diameter of the particle, where λ is the wavelength of the light.

2.1.1 Optical Forces in Rayleigh Regime (d << λ)

This is the regime where particle diameter is very small compared to the wavelength. Since the particle size, d, is smaller than the wavelength of the trapping beam, the particle essentially sees a stationary field. That means, the phase of the field is constant in time. Thus, the photons are treated as waves in this picture. The particle can be considered as an induced dipole.

The magnitude of the scattering force is proportional to the optical intensity. The direction of this force is the same with the incident light. The scattering force is generally defined as

$$F_{scat} = \frac{n_b P_{scat}}{c} \tag{2.1}$$

where n_b is defined as the refractive index of the medium and P_{scat} is the power of scattered photons. The scattering cross section for Rayleigh particles [61] is

$$\sigma_{scat} = \frac{2\lambda^2}{3\pi} k^6 \left(\frac{m^2 - 1}{m^2 + 2}\right)^2 \qquad (2.2)$$

where k is the dimensionless size parameter. Using the radius of the particle r, this parameter is defined as

$$k = \frac{2\pi r}{\lambda} \qquad (2.3)$$

The effective refractive index, m, is defined as

$$m = \frac{n_a}{n_b} \qquad (2.4)$$

where n_a is the refractive index of the particle. Large m values result in large surface reflections. For example it is easier to trap polystyrene in water (m = 1,24) comparing to trap them in air (m = 1.65). Using

$$E = I_0 \sigma_{scat} \qquad (2.5)$$

one can find the relationship for scattering force:

$$F_{scat} = \frac{128\pi^5 r^6}{3\lambda^4} \left(\frac{m^2 - 1}{m^2 + 2}\right)^2 n_b \qquad (2.6)$$

The gradient force is proportional to the gradient of optical intensity and propagates in the direction of the gradient of the optical intensity. The gradient force is generally defined as

$$F_{grad} = 4\pi n_b \epsilon_0 a^3 \left(\frac{m^2 - 1}{m^2 + 2}\right) \frac{1}{2} \nabla E^2 \qquad (2.7)$$

where α is the polarizability for a spherical Rayleigh particle [62]. Polarizability of a dielectric spherical particle can be solved by assuming a particle with radius r, refractive index n_p in a medium of refractive index n_b and an external field E. Following the solution steps [63], the polarizability is found to be

8

$$\alpha = n_b r^3 \left(\frac{m^2 - 1}{m^2 + 2}\right) \tag{2.8}$$

The gradient force can be found using this result as below [62]:

$$F_{grad} = 4\pi\epsilon_0 \frac{n_b^2 r^3}{2} \left(\frac{m^2 - 1}{m^2 + 2}\right) \nabla < E^2 > \tag{2.9}$$

2.1.2 Forces in Mie Regime (d >>λ)

Incident beam on the test particle can be considered as simple rays in Mie regime since the diameter of the particle is far bigger than the wavelength of the light. Due to Snell refraction law and Fresnel formulas, the ray optical description of the optical forces exerting on a dielectric sphere can be demonstrated as in figure 2.1. In this figure two beams are demonstrated, A and B. These beams stem from the different intensity gradient regions of the beam, which means the force they exert on the particle is different. The momentum of the rays are denoted as p in the figure.

The ray optical derivation of the forces in Mie regime was made by Ashkin and his colleagues in 1992 [64]. In this study, the net force on the dielectric sphere was found by summing the contributions from each the ray entering the aperture of radius r with respect to beam axis and the angle α with respect to y- axis. A sphere close to an intensity gradient was given in figure 2.2.

In this picture, the ray optic calculations are made using the Fresnel transmission and reflection coefficients T and R. As a result, the contributions of rays that followed sequential reflections and transmissions were calculated as below:

$$F_Z = F_{scat} = \frac{n_1 P}{c} \left\{ 1 + R\cos2\theta - \frac{T^2[\cos(2\theta - 2r) + R\cos2\theta]}{1 + R^2 + 2R\cos2r} \right\} \tag{2.10}$$

$$F_Y = F_{grad} = \frac{n_1 P}{c} \left\{ R\sin2\theta - \frac{T^2[\cos(2\theta - 2r) + R\sin2\theta]}{1 + R^2 + 2R\cos2r} \right\} \tag{2.11}$$

In these equations, P is the power of the beam.

2.1.3 Design of an Optical Tweezers Setup

There are several conditions to achieve a stabile single beam optical tweezers setup. The reflections from the surface of the sphere results in a momentum transfer and that leads the particle to move in the axial direction. That means the scattering forces tend to push the particle from the beam focus. The gradient force must overcome this force to keep the particle in the trap location. Meaning, the beam must be as tight as it can be. One important parameter that defines the beam tightness is numerical aperture. A high numerical aperture objective collects the portion of the beams proportional to this parameter. An efficient high numerical objective generally has the full illumination angle of 70°. Since the formula of the numerical aperture is

$$NA = n \, sin(\alpha) \qquad\qquad (2.12)$$
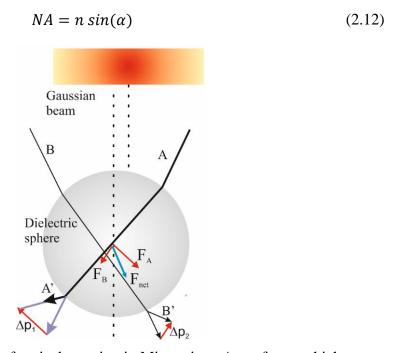
Figure 2.1 : Description of optical trapping in Mie regime. A net force, which stems from the photon momentum transferred, is applied on the dielectric sphere
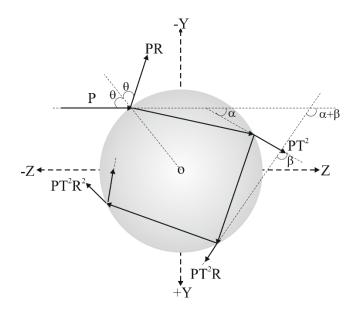
Figure 2.2 : Scheme for the calculation of forces in Mie regime. Beams are described as simple rays and every reflection and refraction contributes R and T coefficients to incoming beam. Vector sum of the rays gives the ray optical calculation of the forces

Typical numerical aperture for water immersion objectives are about 1.20. Fulfilling this aperture is crucial to achieve optical tweezers. Besides, the refractive index of the particle must be as close as possible to the refractive index of the material it is in. Otherwise, the refracted rays tend to push the particle out of the beam focus. To summarize the conditions:

- Tight beam
- High numerical aperture
- $F_{grad} > F_{scat}$
- Small value of m

A typical experimental setup for single beam optical tweezers is shown in figure 2.3.
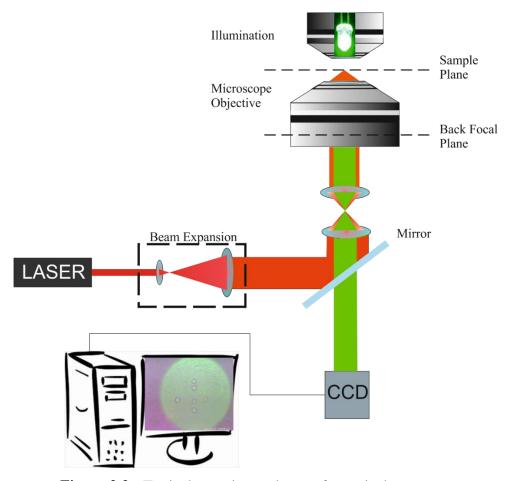
Figure 2.3 : Typical experimental setup for optical tweezers.

A Keplerian telescope system consisting of two plano-convex lenses magnifies the beam diameter as many as the ratios of the focal lengths of the lenses f_2/f_1. The magnified beam is collimated into the back aperture of the microscope objective. The high numerical objective allows the tight focus. The sample that includes test particles in suspension is illuminated with this beam and the trapped particles are monitored via a CCD camera. The choice of wavelength may depend on what one aims to trap. Since photo damage is a big concern for biological particles, near infrared wavelengths (e.g. 785 nm, 1064 nm) are more appropriate for such applications since the energy transferred to the sample is more acceptable in this region.

2.2 Spatial Light Modulators

Spatial light modulators are devices that change the phase of the incident light on the active area of the LC display by changing voltage applied on the liquid crystal molecules. These devices have various applications in several research fields. In the

last two decades, they found use in optical tweezers setups for the purpose of programmatically generate traps and move them both laterally and axially.

The structure of these devices is called LCoS (liquid crystal layer on silicon substrate). Liquid crystal (LC) is a mesophase of material, which means it may behave like liquid, solid, or both by means of molecule order parameters, flow characteristics, and physical state depending on the medium conditions. Liquid crystal can mainly be grouped in two: Thermotropic and lyotropic. Additionally, liquid crystalline phases can be classified as nematic, smectic, cholesteric, and columnar. In nematic LC, rod shaped molecules are almost parallel to each other. A unit vector is described in the direction of average orientation of the long axis and is called director. This vector points the direction where most LC molecules tend to point. The deviation from this vector describes the order parameter of the LC. There is a special kind of nematic phase called twisted nematic phase. In this effect, nematic crystal molecules are confined between two plates, glasses and polarizers. The molecules are naturally twisted when there is no electrical field applied. An incident light first passes through the first polarizer, and then the polarization of the light is rotated due to twisted LC molecules. The beam is let out through the second polarizer whose polarization angle is adjusted 90° with respect to the first one. When a small electric field is applied on, the LC molecules of twisted nematic phases realigned as seen in figure 2.4.
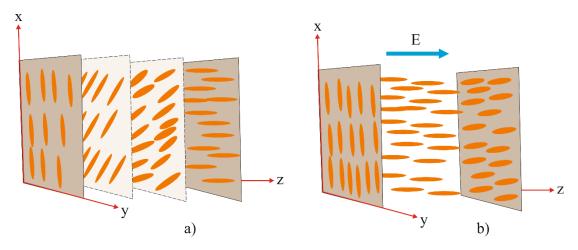
Figure 2.4 : Twisted nematic (TN) LC phase when the external field is a) off and b) on.

Smectic LCs are ordered in more than one dimension because of its layered structure. Chiral nematic crystals also known as cholesteric LCs apply intermolecular forces at a small angle to each other. These forces make the material visualized as stack of two-

dimensional layers showing properties similar to nematic crystals. The phases of the liquid crystals are summarized in figure 2.5.

Nematic Phase **Smectic Phase** **Cholesteric Phase (Chiral Nematic Phase)**
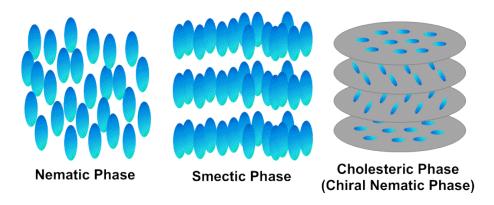
Figure 2.5 : Liquid crystal phases [65].

LCs have the property of birefringence, double refractive index, that is useful for phase modulation. LCoS devices are generally made of ferroelectric or twisted nematic (TN) LCs. Both have their own advantages. Ferroelectric devices work in two states while TN-LCs have as many as 256 or 512 states between $0 - 2\pi$. Ferroelectric devices work much faster than TN-LCs. Researchers in HOT applications mostly choose TN-LC devices because of its flexibility [66].

2.2.1 Phase Modulation

The phase modulation in SLMs is performed, basically, by changing the voltage of each cell. The operation of the device generally obeys the equation 2.13:

$$\overrightarrow{E_{out}} = M_{SLM}\overrightarrow{E_{in}} \tag{2.13}$$

Here, M_{SLM} is the matrix element representing Jones matrices which was originally introduced by R. C. Jones in 1941 [67]. The eigenvectors of this element has to be found for each specific case e.g. illumination with linear polarized light. In the phase mostly devices, which is also used in this study, illuminating the SLM with linearly polarized light is sufficient for a good diffraction efficiency.

The liquid crystal on silicon (LCoS) SLM is a birefringent device. Such devices have two refractive indices. One is n_e (e for extraordinary) and the other is n_o (o for ordinary). The angles of the LC molecules vary with the voltage applied on the device. This directly leads to a phase shift in the output with the relation as in equation 2.15 [66]:

$$\Delta\phi = \frac{2\pi}{\lambda}(n_e - n_o)d \tag{2.14}$$

This equation reads the principle of phase modulation: Wave front transformation is achieved by changing of electric field performed on the LC layer. Final alignment of LC molecules provides the reflected, therefore, transformed wave front.

2.2.2 SLM Types and Specifications

SLM is a device that is able to change some properties of an optical wave front. There are two kinds of SLMs according to their addressing schemes: Electrical and optical. LCoS devices use electrical addressing that relies on converting electrical data, commonly obtained from DVI or VGA ports, to optical information. Fig. 2.7 shows the diagram of how two addressing schemes works, roughly [68].
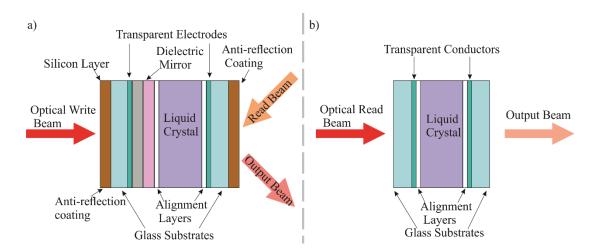
Figure 2.6 : Optical and electrical addressing schemes.

Spatial light modulators can modulate phase, amplitude or both. Phase only spatial light modulators are more efficient since amplitude modulation generally removes a portion of power from the beam and reduces efficiency. Moreover, reflective devices are faster and more effective than the transmissive ones since switching time depends on the thickness of the device and this decreases to its half in reflective SLMs.

Commercial SLMs has several specifications that one needs to consider carefully when choosing an appropriate device. These specifications are shortly explained below:

Pixel Pitch: The pixel pitch is defined as the spatial distance between two pixels of the liquid crystal display.

15

Speed: High frame rate is crucial for a fast hologram computation. The addition of the time for the LC to switch (τ_{LC}) and the time for addressing between the first and last pixel array (τ_{load}) gives the frame rate as in equation 2.17.

$$\tau_{frame} = \tau_{LC} + \tau_{load} \tag{2.15}$$

It is important not to have delays in the frame rate because of addressing or switching.

Fill Factor: Fill factor is a magnitude that determines how much energy is transformed to the zeroth diffraction order. The envelope function that describes how much energy is distributed to the zeroth order is the squared of Fourier transform of the function of a single pixel. Thus, smaller the pixel leads to a better fill factor, therefore, optical efficiency.

A TN, phase only, reflective SLM device was chosen and was purchased from HOLOEYE. The device is 8 bit with 256 gray levels whose resolution is 1920 x 1080, pixel pitch is 8 μm, frame rate is 60 Hz and fill factor is 87%.

2.3 Holographic Optical Tweezers

Efforts to trap more than one particle using single source and single microscope was summarized in the literature section. Usage of DOEs especially SLMs, changed the game dramatically. Programmable LC pixel arrays, SLMs, were used to create multiple traps and manipulate them individually.

First efforts of multiple trapping used AOMs and achieved to trap and laterally manipulate many particles. However, manipulating particles axially needs the control of divergence in the back focal plane of the microscope objective. Doing this using plane using mirrors or AOMs is not possible. These tools were replaced with diffractive optical elements (DOE) about 2 decades ago. Illuminating a grating with a plane wave, diffraction orders will take place in the far field. In the conventional optical tweezers setup, the microscope objective is used as a transform lens. However if, the steering mirror in this setup is replaced with a grating, a linear array of traps are produced. Modifying the period of the grating changes the lateral position of individual traps. If a Fresnel lens is inserted together with the grating, diffraction orders will be shifted out of the far field leading the trap to move axially. After the studies that showed holographic approach that first used superposition algorithms, addressable

DOEs found a wide application around the world. These devices are called spatial light modulators.

To drive these devices using, for example, superposition algorithms, one should create computer-generated holograms (CGH). Creating these phase patterns needs to derive the equations for lateral and axial displacement before superposing them. The theoretical basis of these equations is Fourier optics. These derivations are given in the following section. Updating these holograms real-time due the lateral and axial position of the trapped particles, one can manipulate individual traps just by changing the hologram images displayed on the SLM.

2.3.1 Design of HOT Setup

The standard experimental design for optical tweezers was given in the previous sections. Applying a few modifications on this setup, one can build a HOT experimental setup. The most crucial condition to fulfill here is 4-f configuration. This configuration is demonstrated in figure 2.9.
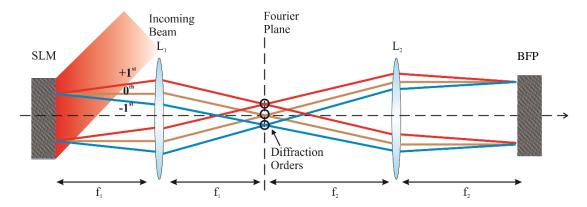
Figure 2.7 : 4-f configuration scheme. Diffractive element, SLM in our case is illuminated with an expanded beam. The image on the SLM is propagated to the image plane using the two lens first of which allows Fourier transform of the image in the Fourier plane and the second creates the inverse Fourier transform of it in the image plane. The image is reconstructed in image plane with no loss comparing to the SLM plane.

It relies on the fact that a lens provides the Fourier transform of the incoming beam in its focal plane. When parallel illuminated, sequence of two lenses will steer the incoming beam towards the back focal plane of the microscope objective with very few losses. Rays with different incident angles on the first lens will be focused to a laterally shifted position in the Fourier plane. The laterally shifted spots in the Fourier plane are imaged in the BFP of the objective lens.

Applying this condition for the optical tweezers setup, after the addition of two lenses and SLM, the common HOT experimental setup is obtained as displayed in figure 2.10. In this setup, the Keplerian telescope system expands the laser beam to fully illuminate the SLM which displays a computer generated hologram on its surface. The SLM is positioned in the object plane of the Fourier lens of the second telescope. The reflected light from the SLM includes higher diffraction orders. The common practice is to block higher order and zeroth order beams and propagate the first diffraction order beams to the back focal plane of the microscope objective. The lens in front of the SLM creates the Fourier transform of diffracted beams and images them in the back plane of the second lens, which is also called Fourier plane. This complex beam is imaged onto the back aperture of the microscope objective via combination of lenses. Since the SLM plane and the back aperture of the objective lens is conjugate planes, possible walk-off of the higher diffraction order beams are prevented. Moreover, the second telescope creates a mathematical relationship between the beam at the output of the hologram and the beam in the focal plane since these planes are conjugate planes. These lenses limit the beam diameter and provide the desired beam diameter in the BFP needed for optical tweezers.
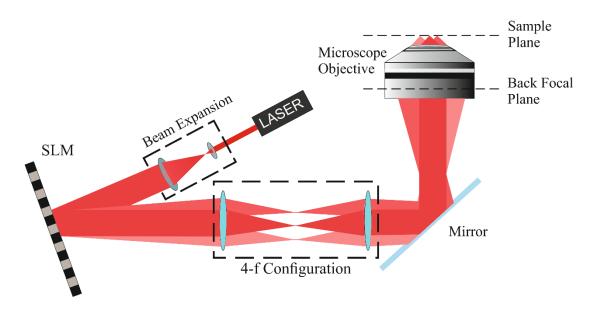
Figure 2.8 : Typical HOT setup.

Without a beam block element, all diffraction orders are propagated to the microscope back focal plane together with the zeroth order beam. The higher order beams are generally eliminated using an aperture in the Fourier plane, which is located between

Fourier lens and objective lens and is the place where the diffraction orders are optically well separated. In such cases, the second telescope system behaves as a spatial filter. The zeroth order beams can be eliminated using a beam block [69] or an adapted hologram algorithm [70].

2.3.2 Algorithms

Computer generated holograms that are essential in holographic optical tweezers. They are phase patterns displayed on the DOEs in order to manipulate individual traps laterally and axially.

Algorithms of phase pattern generation stem from the Fourier optics principals. It would be more elucidatory to start from these derivations which were adapted from J. Goodman's book on Fourier optics [71] and Persson's Phd thesis [72].

According to scalar diffraction theory, an electromagnetic field illuminating the SLM plane is assumed as a scalar field. Propagating the field to the back aperture of microscope objective may be in two ways: As demonstrated in figure 2.11 where the field in plane A is propagated to plane B a) using a lens b) in free space.
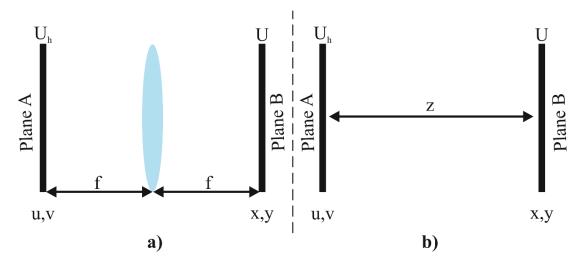
Figure 2.9 : Propagation from plane A to B with a) Fourier transform using a lens b) Fresnel diffraction

Here, two planes are conjugate planes and the field displayed on plane B is Fourier transform of the field on plane A. The equation of Fourier hologram providing this propagation is given below:

$$U(u,v) = \frac{1}{\lambda f} \iint\limits_{-\infty}^{\infty} U_0(x,y) \exp\left(-i\frac{2\pi}{\lambda f}(ux+vy)\right) dxdy \qquad (2.16)$$

The other possibility is that the field in plane A is propagated to plane B which is separated from the former one with a distance z without using any lenses. This kind of propagation is calculated with Rayleigh-Sommerfeld diffraction integral. The expression that is used in these situations is given as:

$$U(u,v,z) = \frac{1}{i\lambda} \iint\limits_{-\infty}^{\infty} U_0(x,y,0) e^{ikr} \frac{\cos(\theta)}{r} dxdy \qquad (2.17)$$

For long optical distances $(z \gg f)$, some simplifications regarding to paraxial approximation can be done using

$$r = \sqrt{z^2 + (x-u)^2 + (y-v)^2} = z\sqrt{1 + \frac{(x-u)^2 + (y-v)^2}{z^2}} \qquad (2.18)$$

Binomial expansion of the above expression produces:

$$r \approx z + \frac{1}{2}\frac{(x-u)^2 + (y-v)^2}{z} \qquad (2.19)$$

Placing this in the Rayleigh-Sommerfeld equation together with $\frac{\cos(\theta)}{r} = \frac{z}{r^2} \approx \frac{1}{z}$, Fresnel diffraction integral given in equation 2.22 is obtained.

$$U(u,v,z) = \frac{e^{ikz}}{i\lambda z} \iint\limits_{-\infty}^{\infty} U_0(x,y,0) e^{\frac{ik}{2z}\{(x-u)^2 + (y-v)^2\}} dxdy \qquad (2.20)$$

The incident beam is propagated, first, from the SLM to the front plane of the Fourier lens. Then, it transmits through the lens and finally, the beam propagates from the back plane of the Fourier lens to the back focal plane of the microscope objective. The field in the front plane of the lens is

$$U(u',v',f) = \frac{e^{ikf}}{i\lambda z} \iint\limits_{-\infty}^{\infty} U_{SLM}(x,y) e^{\frac{ik}{2f}\{(x-u')^2 + (y-v')^2\}} dxdy \qquad (2.21)$$

20

Using the thin lens approximation, the field in the back plane of the lens is provided by multiplication of the field in the front plane by $e^{-\frac{ik}{2f}(u'^2+v'^2)}$:

$$U(v', u', f) = \frac{e^{ikf}}{i\lambda z} \iint\limits_{-\infty}^{\infty} U_{SLM}(x,y) e^{\frac{ik}{2f}(x^2+y^2)} dx dy \qquad (2.22)$$

The field in the back focal plane of the microscope is calculated by multiplication of the Fresnel diffraction integral of the field in the back plane of the Fourier lens to target plane of the objective by the field in the back plane of the Fourier lens. Since the distance to target plane from backplane of the lens is f+w, the variable z is replaced with this value when calculating the Fresnel integral. Combining these, the field in the target plane is calculated as

$$
\begin{aligned}
&U_{BFP}(u, v, w) \\
&= \frac{e^{\frac{i2\pi(2f+w)}{\lambda}}}{i\lambda f} \iint\limits_{-\infty}^{\infty} U_{SLM}(x, y, 0)\, e^{-i\frac{\pi w}{\lambda f^2}(x^2+y^2)} e^{-i\frac{2\pi}{\lambda f}(ux+vy)} dx dy
\end{aligned}
\qquad (2.23)
$$

In HOT setup, it is aimed to propagate the electromagnetic field on the SLM to microscope back focal plane without changing the space, e.g. lateral distance changes in SLM plane should produce the same changes in sample plane as demonstrated in figure 2.12.
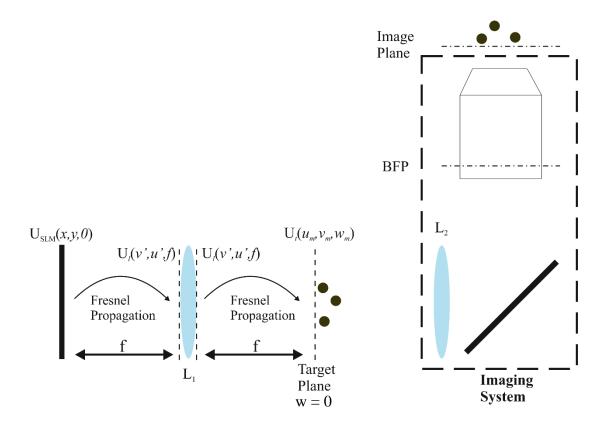
Figure 2.10 : Propagation of electromagnetic field from SLM plane to sample plane.

CGH application needs numerical procedures, which consist discrete iterations of operations. Thus, equation 2.23 is discretized given in 2.24.

$$U_{BFP}(u,v,w) = \frac{e^{\frac{i2\pi(2f+w)}{\lambda}}}{i\lambda f} \sum_{x,y} U_{SLM}(x,y) \, e^{-i\left(\frac{\pi w}{\lambda f^2}(x^2+y^2)+\frac{2\pi}{\lambda f}(ux+vy)\right)} \qquad (2.24)$$

Generally, a complex field in the BFP can be written as

$$U_{BFP}(u,v,w) = \frac{e^{\frac{i2\pi(2f+w)}{\lambda}}}{i\lambda f} \sum_{x,y} |U_{SLM}(x,y)| \, e^{-i\left(\phi_j - \Delta_j^m\right)} \qquad (2.25)$$

Where ϕ_j is the corresponding phase shift for the field in j[th] pixel and f is the focal of the Fourier lens. The phase shift for m[th] trap is on j[th] pixel is:

$$\Delta_j^m = \frac{\pi w}{\lambda f^2}\left(x_j^2 + y_j^2\right) + \frac{2\pi}{\lambda f}\left(u_m x_j + v_m y_j\right) \qquad (2.26)$$

A more compact notation can be made by writing the dimensionless variable u as in equation 2.27.

$$U_m = \sum_{j=1,N} \frac{1}{N} e^{-i\left(\phi_j - \Delta_j^m\right)} \tag{2.27}$$

Where

$$I_m = |U_m|^2 \tag{2.28}$$

is satisfied for the energy flux through a diffraction limited spot whose surface is $f^2 \lambda^2 / Nd$. While building the algorithms, the main task is to look for the optimum ϕ_j that will maximize the modulus of u_m for a given set of Δ_j^m. The performance parameters are efficiency, uniformity, and standard deviation.

$$e = \sum_m I_m \; ; \; u = 1 - \frac{\max(I_m) - \min(I_m)}{\max(I_m) + \min(I_m)} \; ; \; \sigma = \frac{100\sqrt{< (I - < I >)^2 >}}{< I >} \tag{2.29}$$

The efficiency defines how much intensity is distributed in the image plane comparing to the incoming beam intensity on the SLM. Uniformity defines how the trap intensities are distributed. It approaches to one as the the trap intensities get closer while the standard deviation in the intensities increase, it approaches to zero.

2.3.2.1 Gratings and Lenses Algorithm

This algorithm is a superposition algorithm where the amplitude part of the hologram is not taken into account. Traps are created and manipulated with a good accuracy using a phase only hologram. As discussed above, lateral movement of the traps are considered as light is diffracted from a grating to cause this movement and axial movement of the traps is considered as a Fresnel lens is replaced with this grating. When multiple traps are considered, total hologram is calculated as a sum of individual phase holograms. First, the dimensionless field u_m must be maximized as discussed in the previous section [73].

$$\frac{\partial}{\partial j}\sum_m Re\left\{U_m\right\} = Re\left\{\frac{ie^{i\phi_j}}{N}\sum_{m=1,N}e^{-i\Delta_j^m}\right\} = 0 \tag{2.30}$$

The solution for the phase is as below:

$$\phi_j = arg\left[\sum_{m=1,N}e^{i\Delta_j^m}\right] + n_j\pi, \qquad n_j = 0,1 \tag{2.31}$$

The Hessian matrix applied on this equation has to be negative definite for the stationary point to be local maximum.

$$\frac{\partial^2}{\partial\phi_j\partial\phi_k} = \sum_{m=1,N}Re\{U_m\}|_{\phi_j=\overline{\phi_j}} = -\delta_{jk}(-1)^{n_j}\left|\frac{1}{N}\sum_m e^{i\Delta_j^m}\right| \tag{2.32}$$

One obtains the maximum condition for $n_j = 0$. Then

$$\phi_j = arg\left[\sum_{m=1,N}e^{i\Delta_j^m}\right] \tag{2.33}$$

Mapping these phase arguments and displaying it on the SLM will quickly provide traps for **Gratings and Lenses** algorithm.

2.3.2.2 Gerchberg-Saxton Algorithm

Gerchberg-Saxton algorithm was founded by two crystallographers Ralph Gerchberg and Owen Saxton [74]. This algorithm includes amplitude component of the field, too. The field is propagated back and forth from the SLM plane to trapping plane sing fast Fourier transforms. In each step, the algorithm takes care of the amplitude distributions to be satisfied after transformations.

Implementing a 3D manipulation with these algorithms is costly of CPU times. That means it is not possible to use it for real time applications. However, some simplifications can be done in HOT applications. Discretizing the algorithm to reform

the amplitude only in the trap locations, the similar optimization problem in the gratings and lenses algorithm is reached.

$$\frac{\partial}{\partial j}\sum_m |u_m| = Re\left\{\frac{ie^{i\phi_j}}{N}\sum_{j=1,N} e^{-i\Delta_j^m}\frac{u_m^*}{|u_m|}\right\} = 0 \tag{2.34}$$

$$\phi_j = arg\left[\sum_{j=1,N} e^{i\Delta_j^m}u_m/|u_m|\right] + n_j\pi, \qquad n_j = 0,1 \tag{2.35}$$

The Hessian matrix is not diagonal when calculated for the above equation.

$$\frac{\partial^2}{\partial\phi_j\partial\phi_k} = \sum_{j=1,N} Re\{u_m\}|_{\phi_j=\overline{\phi_j}}$$

$$= -\delta_{jk}(-1)^{n_j}\left|\frac{1}{N}\sum_m e^{i\Delta_j^m}\frac{u_m^*}{|u_m|}\right| + O\left(\frac{1}{N^2}\right) \tag{2.36}$$

As discussed in [42], non-diagonal terms are $1/N$ times smaller than the diagonal terms. This kind of perturbation can only change the sign the sign of the eigenvalue. For large values of N, this can be neglected and the stationary phase equation will be:

$$\phi_j = arg\left[\sum_{j=1,N} e^{i\Delta_j^m}u_m/|u_m|\right] \tag{2.37}$$

In this equation, ϕ_j is the phase of the linear superposition of single-trap holograms with coefficients of unit modulus u_m is the field of the m$^{\text{th}}$ trap produced by ϕ_j. The equation is, now, dependent on the field unlike superposition algorithms. A simple approach to make the numerical calculations of phase images, one might guess an inital phase obtained from gratings and lenses algortihm and use the above eqation in an iterative procedure.

2.3.2.3 Random Mask Algorithm

When the number of traps is more than one, an algorithm that is computationally more compact and that takes care of the amount of field distribution on the traps is needed. Random mask algorithm chooses random pixels on the SLM, which divides the screen in domains as many as number of traps as described in Montes-Usategui *et. al* [75].

The phase pattern of the algorithm is very simple as given below:

$$\phi_j = \Delta_j^{m_j}$$

(2.38)

This results in very fast for realization of video rate trap manipulation. However, the efficiency is reduced as the number of traps increase. As suggested in [42], this algorithm can be useful to create additional traps to quickly help other algorithms that work slower in comparison with this algorithm. This is Random Mask algorithm is sometimes defined as "helper tweezers".

2.3.2.4 Direct Search Algorithm

Above discussed traps have the advantages of being quickly adapted to software, general and sometimes the speeds are close to the video rates. However, they are also claimed to distribute unexpected laser power into the sample plane and to transfer most of the input power to ghost traps (unwanted spots in the sample that have enough intensity to trap particles) [76]. To overcome this, direct search algorithm is suggested. In this algorithm, one starts from a good guess (phase image) calculated using a low-computational-cost algorithm such as superposition algorithms. Then, every 256 grayscale pixel is scanned one by one to check if the cost function is improved. Here, the cost function is,

$$C = \frac{e}{M} - f\sigma$$

(2.39)

where f is the weighting fraction and sets the relative importance to diffraction efficiency compared to uniformity. Uniformity is maximum (1.00) when f = 0.5 is provided.

2.4 Raman Spectroscopy

As C.V. Raman suggested [19], when an incoming photon strikes a molecule in the sample, some part of the light is absorbed or transmitted. Remaining part of the beam scatters from the molecules in the sample. Scattered photons make transition between vibrational energy levels. Two kinds of scatterings are observed: Elastic and inelastic. Most of the photons are scattered elastically and this is called Rayleigh scattering where the ground vibrational energy level is excited to upper level and relaxes to the same level. About one in a million photons, an inelastic scattering is observed. In this

kind of scattering, the scattered photons are either redshifted or blue shifted. The amount of these shifts is equal and it corresponds to the vibrational frequency of the molecule that is excited. The scattering mechanism that produces redshifted photons is called Stokes scattering and blue shifted one is called Anti-Stokes.. Due to the Maxwell-Boltzman distribution, the population of the excited level in Stokes scattering is higher. Thus, Stokes Raman signal intensity is higher comparing to Anti-Stokes.

In Raman experimental setups, the scattered photons are collected into a monochromator with the help of a dispersive optical element (such as prism or grating) and are converted to electronic signal thanks to charge-coupled detectors (CCD). Since the origin frequency is adjusted to Rayleigh frequency, the x-axes of the spectra are called Raman shift and this quantity is exactly equals to the molecular vibration frequency. This is why Raman spectroscopy is called a "fingerprint spectroscopy". Using Raman spectroscopy, one can measure solids, liquids, and gases.

2.4.1 Semi Classical Theory

One of the above discussed terms, vibrational frequency, can be formulized if one considers a diatomic molecule as in Figure 2.13 to describe the vibrational frequency of a molecule. Since the fundamental of Raman, spectroscopy relies on molecular vibrations, a hypothetical spring is assumed between two atoms of a molecule. The restoring force should verify the motion equation in one direction. The derivations below are adapted from Ferraro *et.al* [77].
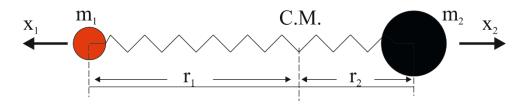
Figure 2.11 : Diatomic molecule

The equation of the diatomic system according to the center of mass can be written as in equation 2.40:

$$m_1 r_1 = m_2 r_2 \tag{2.40}$$

The displacement variables x_1 and x_2 are obtaine using the equilibrium points in eq. 2.40.

$$m_1(r_1 + x_1) = m_2(r_2 + x_2) \tag{2.41}$$

$$x_1 = \frac{m_2}{m_1} x_2 \tag{2.42}$$

Using Hooke's Law and equation of motion equations 2.43-46 are derived.

$$F = -K(x_1 + x_2) \tag{2.43}$$

$$F = -K \left(\frac{m_1 + m_2}{m_1} \right) x_2 = -K \left(\frac{m_1 + m_2}{m_2} \right) x_1 \tag{2.44}$$

$$m_1 \ddot{x}_1 = -K \left(\frac{m_1 + m_2}{m_2} \right) x_1 \;\; ; \;\; m_2 \ddot{x}_2 = -K \left(\frac{m_1 + m_2}{m_1} \right) x_2 \tag{2.45}$$

$$\left(\frac{m_1 m_2}{m_1 + m_2} \right) \ddot{x}_1 + K x_1 = 0 \;\; ; \;\; \left(\frac{m_1 m_2}{m_1 + m_2} \right) \ddot{x}_2 + K x_2 = 0 \tag{2.46}$$

Defining effective mass, angular frequency, and effective displacement in equation 2.47, one can solve differential equation for the effective position vector of diatomic molecule given below in equations 2.48 - 2.51.

$$\mu = \left(\frac{m_1 m_2}{m_1 + m_2} \right); \quad w^2 = \frac{K}{\mu}; \quad q = x_1 + x_2 \tag{2.47}$$

$$(\ddot{x}_1 + \ddot{x}_2) + w^2(x_1 + x_2) = 0 \tag{2.48}$$

$$\ddot{q} + w^2 q = 0 \tag{2.49}$$

$$q = q_0 \sin(2\pi v_0 t + \varphi) \tag{2.50}$$

$$v = \frac{1}{2\pi} \sqrt{\frac{K}{\mu}} \tag{2.51}$$

Here, q_0 is the maximum displacement, ν_0 is the classical vibrational frequency, and φ is the phase constant. The total classical energy for vibrational levels can also be calculated using the mechanical energy formula:

$$E = T + V \tag{2.52}$$

$$E = \frac{1}{2}\mu \dot{q}^2 + \frac{1}{2}Kq^2 \tag{2.53}$$

$$E = 2\pi^2 \nu_0^2 \mu q^2 = constant \tag{2.54}$$

However, this energy profile is parabolic which is not consistent with the practical case. Quantum mechanical correction to this potential is introduced. Harmonic oscillator energy eigenvalue:

$$E_v = h\nu(v + \frac{1}{2}) \tag{2.55}$$

This means the lowest energy value is $\frac{h\nu}{2}$. In classical parabolic potential, this value is zero! Moreover, due to tunnel effect, a probability to find q outside the potential curve must exist. This is also not applicable in classical potential. Additionaly, the quantum mechanical rule for energy separation of $h\nu$ is not applicaple in classical potential. Instead of this, Morse potential is suggested whose formula is given below:

$$V = D_e\left(1 - e^{-\beta q}\right)^2 \tag{2.56}$$

Where D_e is the dissociation energy and β is a coefficient for the curvature of the potential well. The new eigenvalue of the Schrodinger equation for anharmonic oscillator is

$$E_v = hc\omega_e\left(v + \frac{1}{2}\right) - hc\chi_e\omega_e\left(v + \frac{1}{2}\right)^2 + \cdots \tag{2.57}$$

To find the origin of Raman spectroscopy, one can model an oscillating electromagnetic field with a frequency of ν_0, interacting with a molecule whose vibration frequency is ν_m. The equation related to this electromagnetic field is given in 2.58.

$$E = E_0\cos(2\pi\nu_0 t) \tag{2.58}$$

When this field interacts with the sample, therefore the molecules, an electric dipole P is induced:

$$P = \alpha E = \alpha E_0 \cos(2\pi\nu_0 t) \tag{2.59}$$

In the equation above, α is polarizability. For small amplitude vibration, this quantitiy becomes function of displacement, q. The polarizability can be expanded with the Taylor series as in equation 2.60.

$$\alpha = \alpha_0 + \left(\frac{\partial\alpha}{\partial q}\right)_0 q + \cdots \tag{2.60}$$

Keeping in mind the nuclear displacement is

$$q = q_0 \cos(2\pi\nu_m t) \tag{2.61}$$

Placing 2.60 and 2.61 in 2.59, the final equation for dipole moment becomes:

$$P = \alpha_0 E_0 \cos(2\pi\nu_0 t) + \left(\frac{\partial\alpha}{\partial q}\right)_0 q_0 \, E_0\cos(2\pi\nu_m t) \, \cos(2\pi\nu_0 t)$$

$$= \alpha E_0 \cos(2\pi\nu_0 t) + \tfrac{1}{2}\left(\frac{\partial\alpha}{\partial q}\right)_0 q_0 E_0\{\cos[2\pi(\nu_0 - \nu_m)t] + \cos[2\pi(\nu_0 + \nu_m)t]\,\} \tag{2.62}$$

Rayleigh   Stokes   Anti-Stokes

This equation defines the scattered beams theoretically, which were given as plain formulas in the introduction section. Explanation that is more concise is made using a Jablonski diagram in Figure 2.14.
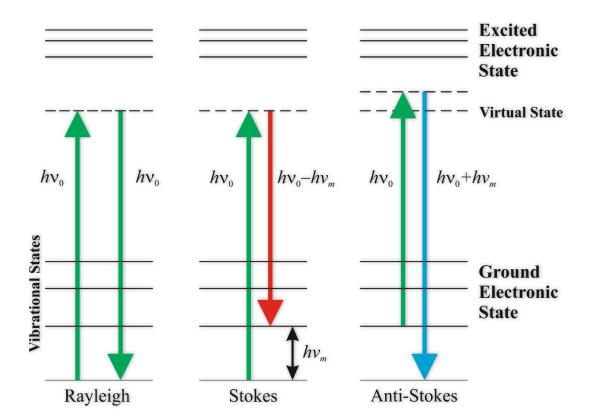
Figure 2.12 : Jablonski diagram for electronic and vibrational transitions in molecules. The solid lines at the bottom represent vibrational states of the ground electronic state. Similarly, the lines at the top represent the vibrational states of the excited electronic state. As seen from the Stokes and Anti-Stokes transitions, the scattered light whether blue shifts or red shifts in Raman scattering.

As it is seen in this diagram, a molecule excited to a virtual state by a photon can respond in three ways: First, the molecule can emit a photon of equal energy of the incident photon after it relaxes back to ground state. This one is called Rayleigh scattering. Second, the molecule can go back to a real phonon state. This time it emits a photon with less energy than the incident photon and this is called Stokes scattering. Third, molecule is already in an excited phonon state, is excited to a higher virtual state, and then relaxes back down to the ground state emitting a photon with more energy than the incident photon. This is called Anti-Stokes scattering. Most molecules are found in the ground state at room temperature according to Maxwell-Boltzmann distribution given in equation 2.63.

$$\frac{N_{excited}}{N_{lower}} = \frac{g_{excited}}{g_{lower}} e^{\left\{ -\frac{(E_{excited} - E_{lower})}{kT} \right\}} \tag{2.63}$$

In this equation $g_{excited}$ and g_{lower} are the state degeneracies of the lower and excited vibrational energy levels. Thus, there is a lower probability for a photon to be Anti-

Stokes scattered. That is why most Raman measurements, including our studies, consider only the Stokes shifted light. The intensity of the Stokes scattering can be derived from the Hertzian dipole as

$$I_{stokes} = KI_0(\nu_0 - \nu_m)^4 \alpha^2 \tag{2.64}$$

Another concept that equation 2.62 tells us is, if the polarizability varies with respect to displacement of the molecule, then the molecule is Raman active. Actually, to define a molecule Raman active, a polarizability ellipse is generally used to define the Raman activity. If the polarizability ellipse changes during vibration, the molecule is defined as Raman active.

2.4.2 Quantum Mechanical Description of Raman Spectroscopy

Raman scattering is explained by the Kramers-Heisenberg-Dirac (KHD) equation in quantum mechanics. In this theory, the mechanism is described as an excitation to a virtual state lower in energy than a real electronic transition with nearly coincident de-excitation. As a result, there will be a change in vibrational energy.

In KHD theory, polarizability tensor α is expanded and is described with the relation below:

$$\left(\alpha_{\rho\sigma}\right)_{fl} = \sum_r \left\{ \frac{< f|\mu_\rho|r >< r|\mu_\sigma|l >}{\hbar\omega_{rl} - \hbar\omega_0 - i\Gamma_r} + \frac{< f|\mu_\sigma|r >< r|\mu_\rho|l >}{\hbar\omega_{rf} - \hbar\omega_0 - i\Gamma_r} \right\} \tag{2.65}$$

where l is the initial state, f is the final state, r represents the eigenstates of molecule, σ is the polarization of incident light, ρ is the polarization of Raman light, $\left(\alpha_{\rho\sigma}\right)_{fl}$ is polarizability tensor component (ρ, σ) for transition $f \leftarrow l$, ω_0 is the angular frequency of incident beam, ω_{rl} is the angular frequency for transitions $r \leftarrow l$, Γ_r is the damping factor related to lifetime of states r, μ is the dipole moment operator, and $\hbar$ represents $h/2\pi$ where h is Planck's constant.

In order to make clear interpretations out of KHD equation, some simplifications can be made using Born-Oppenheimer approximation. This approximation states that, the wave functions of the eigenstates are separated into electronic and vibronic terms involving nuclear and electronic co-ordinates since the electronic transitions occur

much faster than the vibronic transitions of the nuclei. Thus, the wave function of an eigenstate can be written as:

$$\psi = \lambda_{(a,A)} \theta_{(A)} \tag{2.66}$$

where a is the electronic coordinate, A is the nuclear coordinate, λ is the electronic wavefunction, and θ is the vibronic wave function. Including this expression into KHD equation will produce equation 2.67:

$$< r|\mu|l > = < \theta_{(A)_r} \lambda_{(a,A)_r} |\mu| \lambda_{(a,A)_l} \theta_{(A)_l} > \tag{2.67}$$

This equation can be re-written as

$$< r|\mu|l > = \underset{\text{Electronic State}}{\underline{< \lambda_{(a,A)_r} |\mu| \lambda_{(a,A)_l} >}} \underset{\text{Vibronic State}}{\underline{< \theta_{(A)_r} |\mu| \theta_{(A)_l} >}} \tag{2.68}$$

The electronic state part of the equation can be integrated over electronic coordinates, a will produce A dependent M_{rl_A} matrix element of the overlap integral also known as oscillator strength is given in equation 2.69.

$$M_{rl_A} = < \lambda_{(a,A)_r} |\mu| \lambda_{(a,A)_l} > \tag{2.69}$$

Since the matrix elements are functions of inter-nuclear coordinates of A, one can expand the equation 2.70 in Taylor series around equilibrium point A_0.

$$M_{rl} = M_{rl_{A_0}} + \left(\frac{\partial M_{rl}}{\partial A_\epsilon}\right)_0 A_\epsilon + \cdots \tag{2.70}$$

Where A_ϵ is the normal coordinate operator of vibration mode ϵ. If this equation is applied into the KHD equation, one will obtain:

$$\left(\alpha_{\rho\sigma}\right)_{fl} = A + B + \cdots \tag{2.71}$$

Here, A is Franck Condon term (Albrecht's A term) and represents the zero order term of expansion. This term includes the summation of matrix elements that couples all vibrational states. A is reduced to zero because of orthogonality which means there is no Raman scattering from this component, only Rayleigh scattering.

The term B is called Herzberg Teller term (Albrecht's B term) and describes Raman scattering. This term can be interpreted that no overtones are allowed in Raman spectroscopy. In addition, only symmetric vibrations are allowed in this technique.

2.5 Microfluidics

Microelectromechanical (MEMS) fabrication methods to produce microfluidics devices are well improved after the use of soft lithography in this area. This method suggests fabricate soft polymeric molds replicated from a hard master. The most popular material for the mold is polydimethylsiloxane (PDMS), however another material such as polymethylmethacrylate (PMMA) are used in the literature. Main components used in microfluidics experiments, other than the microfluidic channels, are syringe/pressure pumps, tubings, adaptors and a microscope system to observe the flow. The syringe pump is a motorized system whose displacement is calibrated for specific syringe volumes. They can provide flow rates as small as pL/s. Pressure pumps generate pressure gradients to move the syringe. They can work with multi syringes and they are highly programmable. Syringe pumps are cheap, not too precise, user friendly and can be adapted to too many applications. Pressure pumps are costly, precise, a little complex for simple applications, and they can be used with different solutions at the same time since they come up to four channels depending on the user demand.

The importance of the microfluidics devices is their ability to make experiments in micron size with very small liquid volumes such as picoliters. The advantages of the size reduction are both physical and financial. The devices that have micron size channels will have laminar flow and low Reynolds number. Besides, modeling of biological flow can be done using this miniaturization. Cell culturing [78], concentration measurements [79], disease diagnostic [80] experiments can easily be done with these devices. That is why these devices are also called *lab-on a-chip* devices. Moreover, since the cost of their production is low, mass production of biological kits is made available.

Integration of photonics with microfluidics, also known as optofluidics, opened a new path of investigating biological cells. Single cells are investigated in their environment with the help of detection techniques, which allow the researchers to see inside the cells.

2.6 Multivariate Analysis

Sorting applications in microfluidic channel requires recognizing the every single particle in the channel that is observed. Since the mixture in such channel does not include only the desired types of particles, the software-controlled identification of the particles that are observed needs a machine-learning algorithm evaluated. These are algorithms of multivariate statistical analysis or the ones evolved from them. What is done is to prepare a training set to obtain a linear (or quadratic) model to classify pre-measured samples, and then apply the model on the measurements. The vector length of spectroscopic data is generally huge, as many as CCD detector number or even more after preprocess steps. For example, in our case the matrix size of each measurement in this study is 1024 X 2. After preprocess, a 1640 X 2 vector is obtained. After M measurements, one comes across with a huge matrix to handle with. In this case, the first step must be data reduction and feature exploration, which is made by applying Principal Component Analysis (PCA).

2.6.1 Principal Component Analysis

Physics experiments generally give complex outputs, which include too many measurement variables together with measurement uncertainties, device noises, and other unwanted components. Principal component analysis is a useful non-parametric tool that maximizes signal to noise ratio (SNR) in a measurement to find a new orthonormal coordinate system, which is called principal components. This method reveals the hidden information from huge datasets by reducing their size and selecting the most important features. This property is used in many disciplines such as computer engineering, physics, medicine, psychology.

Measurements in spectroscopy are multivariate since the CCD devices generate wavenumbers as many as the detectors in a row inside the device, e.g. 1024 wavenumbers for 1024 X 256 detector array. Even though not every wavenumber is independent, e.g. peaks consist of several of these; common practice is to name every wavenumber as a variable. Briefly, the initial dataset is reduced to its most important factors as illustrated in figure 2.15.
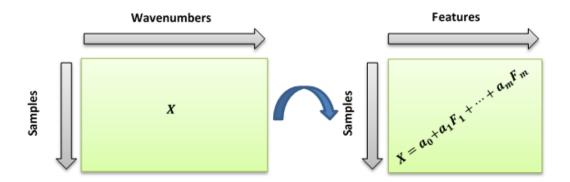
Figure 2.13 : Sampling in PCA.

Here F corresponds to the orthonormal vectors of features and $a_0, a_1 \ldots a_n$ corresponds to the coefficients. This relation is can also be noted as in equation 2.72.

$$X = aF \qquad (2.72)$$

Since the main goal in PCA is to find an orthonormal set where the SNR is maximum, using the covariance matrix Σ of the dataset X is useful. Σ is a square matrice whose diagonal elements are variances of different measurements. Off-diagonal elements are the covariances between different measurements. Now, the problem is reduced to find an orthonormal F matrice where Σ matrice is diagonalized.

This is an eigenvalue problem. There are several ways to solve this. One of the most useful methods is singular value decomposition (SVD). In this algorithm, the dataset X is reconstructed by vector multiplication of the decomposed matrices U, Σ and V where U and V are rectangular matrices and Σ is the square covariance matrix. For spectral data where the matrix is horizontal, the reconstructed matric is obtained after applying SVD as in equation 2.73.

$$X = V\Sigma U \qquad (2.73)$$

$$V^T X^T = U^T \Sigma \qquad (2.74)$$

$$V^T X^T = Z \qquad (2.75)$$

Here V^T is the change of basis from X to Z, which is called scores. U^T is called loading vector in PCA notation. Sorting the scores matrix in descending fashion will give the most significant features of the data. Since the diagonal elements in the Σ matrix are the variance values of the data, the sorted Σ can give the total variance explained values

of each principal component by dividing each variance value by the total variance. This gives the significance of each principle component (PC). Using this information, one can understand how many PCs to use for plotting and classification. After plotting these PCs, the discrimination between the most significant features of the data can be qualitatively observed and the data can be prepared for further analysis such as discrimination or cluster analysis.

Before jumping to SVD, one needs to prepare the data. Mean centering, subtracting the mean from every measurement, is generally the first step. Then, the data is standardized in case some measurements have different physical units. In the spectral analysis case, the data is smoothed, background corrected and/or normalized according to the practitioner's application. A pseudocode for core PCA application is given below:

```
%Prepare dataset as X axis is wavenumbers and Y axis is
measurements
    X = read(x);
    if X axis Measurements
        X = X^T;
    end
%Meancenter and/or standardize data
    X = X - mean(X);
    <X = X/std(X)>

%Apply Spectral Preprocess on the data
    <Background correction>
    <Smoothing>
    <Normalizing>

%Calculate SVD
    [U,S,V] = svd(X);

%Calculate Scores and Loadings
    Scores = V;
    Loadings = U^T;

%Reconstruct Data
    XR = V^T*X;
```

2.6.2 Prediction Ability of the Multivariate Analysis

In a measurement that tests if the samples have a specific condition or not, measurement results give positive or negative outcomes for the condition. The prediction ability of an analysis after a measurement is an important report to understand how well the measurements were classified comparing to the actual

conditions. There are two most common parameter defining this criteria which are called sensitivity and specificity. Sensitivity, is the parameter that predicits the samples that have the condition. Specificity results in the correct prediction of the test for samples that does not have the condition. The summary of the definitons are given in table 2.1.

Table 2.1 : Definitions for sensitivity and specificity.

	Predicted Condition (+)	Predicted Condition (-)	Sensitivity	Specificity
Condition (+)	True Positive (TP)	False Negative (FN)	$\dfrac{TP}{TP + FP}$	$\dfrac{TN}{TN + FP}$
Condition (-)	False Positive (FP)	True Negative (TN)		

2.7 HOT Software

The tasks in holographic optical tweezers are realized via real-time modifying (dynamic) computer generated holograms. A software to fulfill those tasks was developed on Matlab using the hardware in Table 2.1.

Table 2.2 : The computational hardware used in the experiments.

CPU	Intel core i7 4770
Graphics Card	NVidia GTX560 1 GB
RAM	8 GB
Monitor Resolution	1920 X 1080

The software uses the superposition of prisms and lenses algorithm, which was explained in detail above. The software is a graphical user interface (GUI) and allows user to insert as many as the spot he/she wants. The features of the software are summarized below:

- Inserting as many as spots as desired on the screen. Calculate and display the final hologram on SLM screen.
- Controlling the lateral and axial position of the spots by both mouse click and by inserting specific directions.

The main controls on the GUI screen are:

- Insert / Delete spot button.

- Move selected spot to selected X – Y coordinates.

- Move selected spot to desired XY plane (change Z values).

- Update screen coordinates by moving a spot to the reference points of the current image on the screen.

- Obtain Raman signal. Calibrate it.

- Make a quadruple spot on the screen. Move them to Raman coordinates in a loop, obtain signal. The particles are manipulated by updating the computer generated hologram real time when the position of the spot is changed. Apply preprocess and identify the particles. Move them to corresponding channels according to the identification vector. Reposition the array to the initial position after it finishes the movement to the target positions.
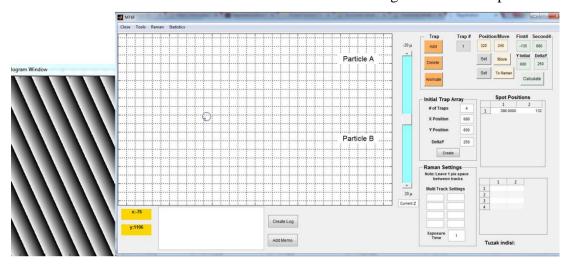
Figure 2.14 : An instant view of the self-written software for HOT. In the figure, it can be seen that a spot and related hologram were created by the software.

When the spots are initially introduced in the screen, related hologram is calculated simultaneously. When the user moves individual particles in three dimensions, the hologram is updated by taking the screen position of the particle as input. Figure 2.16 represents an instant view of the GUI when a spot is inserted in the project.

To understand how prism and lens phases work in optical trapping, figure 2.17 can be looked through. Pictures a and c show holograms for lens and prism phases, respectively. In picture b, 3 traps are manipulated with z = 0. In picture d, 5 traps are trapped and manipulated with $z \neq 0$.
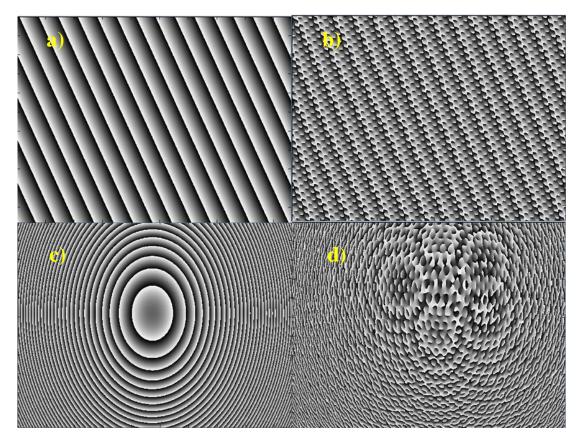
Figure 2.15 : a)Prism phase b) Lens phase. (c) and (d) are holograms for 3 and 6 traps, respectively where spot in (d) are axially shifted from initial position.

2.7.1 Animation Creation

Eight spots are created initially by the computer-generated holograms. The animation is supposed to work like a production band of a factory. First, the spots are created in the initial points as in figure 2.18. Then, these spots are moved towards eastside of the screen whether they carry a particle or not. When the first set of particles (group of four, vertical direction) reach the point of Raman measurement, software stops movement. The Raman spectrum of particles is obtained during one second. Then according to the identification vector, the particles are moved towards the corresponding channels.

While the first four spots are on their way, other four follows until the first four reaches the final destination. Every group reaching the final destination places themselves in their initial position again. This action happens in infinite cycle until the user presses STOP button.
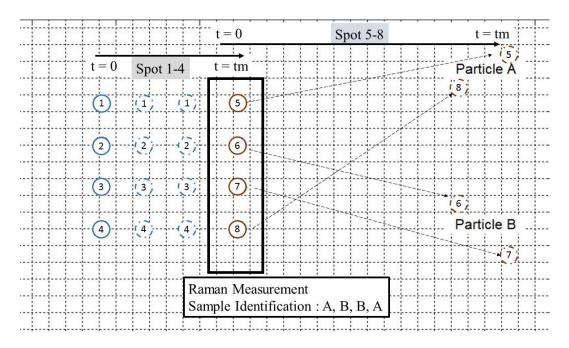
Figure 2.16 : One of the 16 possible pre-calculated paths for the spots generated by HOT software.

2.7.2 Raman Measurement

Raman spectra are taken using the Andor Software Development Kit (SDK) for MATLAB. This kit includes all the MATLAB functions needed to operate our Andor spectrometer and it allows USB connection from monochromator to PC.

When the spots arrive at the measurement point, a multi – track (MT) measurement is obtained. This measurement is set up using MATLAB codes of the SDK. A pseudocode for MT measurement function is given below:

```
Initialize Andor Camera

Configure Acquisition:
*Open CCD Cooler
*Set Acquisition Mode for Single Scan
*Set Exposure Time for 1 second
*Set Read Mode for MT
*Set up MT Tracks
*Set Internal Trigger

Open Shutter, Get Image, Plot

Clean Up and Shutting Down
*Abort Acquisition
*Close Shutter
*Disconnect Andor
```

This code provides monochromator to measure the sample for one second with the user defined MT track settings.

2.7.3 Calibration and Preprocess

Since the measurements the HOT software obtains are uncalibrated, the software performs a wavelength calibration before all the measurements and applies this calibration on them.

The algorithm of the calibration is to fit reference Raman shift values of polystyrene peaks [81] with the pixel values of the current measurement. Here, the fit is the third order and the selected points are not the exact peak points but center of masses of the corresponding peaks. The maximum values of the peaks are requested from user. User picks these points by mouse clicks on the screen. Since these points are not exact points on the spectrum, the closest maximum value to the selected points are found from array. Then the center of mass of this peak is found by Lorentzian peak fitting parameters.

Calculated X values are generally not with equal range and not integer. To get rid of it, Y correspondences of integer X values are found by interpolation. The pseudocode for this process is as below:

```
Request peak positions

Calculate Maximums

Find nearest maximum to selected peaks

Find center of mass of the found peak

Apply 3rd order polynomial fit on center of
masses and reference Raman Shift values

Find the Y correspondence of the integer X values
```

The calibrated spectra are background corrected, smoothed, and normalized, sequentially. Background correction is made automatically according to the article of Lieber *et.al.* [82]. Savitzky – Golay smoothing is applied as a smoothing method. This was applied from MATLAB's routine functions. Vector normalization function was written using the related equation below:

$$X_N = \frac{x_i}{\sqrt{\sum_i x_i^2}} \qquad 2.76$$

Where X_N is normalized data vector, x_i is each number in the raw data vector.

3. EXPERIMENTS AND RESULTS

3.1 Raman Spectroscopy in Medicine

Raman spectroscopy is called a fingerprint spectroscopy, as stated above. Thus, measurements from different samples are unique and each Raman shift gives intrinsic information from the molecular structure of the sample of interest such as protein secondary structure. Using this information together with water giving a low contribution to Raman spectra, Raman spectroscopy appears to be a suitable method for biological/biomedical applications.

During this PhD study, spent culture media where the human embryos are grown were collected from volunteered patients to be investigated in our laboratory. The aim was to find a quantitative way to assess the embryo quality. This study was a collaborative project funded by Istanbul University Scientific Research Fund (project no: 22501) and managed by MD Ercan Baştu from Istanbul University Medical School. A relation between the amount of specific amino acids in the spent culture of embryos and embryo success rate were found to select the best one. The biggest difficulty was the similarities in intensity between the samples of the embryos that could develop to the pregnancy state and the ones that could not. This difficulty had been overcome by applying unsupervised classification methods such as k-means nearest neighbors (KNN).

3.1.1 Embryo Viability Indexing Using Raman Spectroscopy of Spent Culture Media

This study [29] hypothesized that the subjectivity of embryo selection in *in-vitro* fertilization (IVF) can be decreased and the success rate of this process can be increased using Raman spectroscopy and statistical methods. Raman spectra of embryo spent cultures, which are the wastes of the growth medium (G1 medium, Vitrolife) of the embryos, were measured. The samples needed to develop the embryos were drawn from 31 volunteers (16 non-pregnant, 15 pregnant), one from each. The volume of embryo spent culture to be measured were 30 μL in average which needed careful sampling in order to increase the Raman volume as much as possible. Besides,

it is important to prepare bubble-free samples. Considering these necessities, a disk shaped aluminum container, which has a cylindrical hole in the center with a diameter of 1.6 mm was constructed. The length of the hole is 6 mm. This volume of the cylindrical hole in the center is about 16 μL. Both sides of the disk are covered with 1 mm-thick quartz windows. A slit of about 0.5 mm wide was created by getting a piece of disk cut up to let the inside air out.

The measurement setup was built as demonstrated in figure 3.1. The setup uses a 785 nm diode laser source. The source has a power of 100 mW in the output. The beam emitted from the diode laser passes through the Faraday isolator (FI, EOT) which rejects back reflected and backscattered beams and line filter (Semrock) which cleans up the beam profile. The beam transmitted from the line filter is steered to the Raman edge filter (REF, Semrock) by two mirrors.
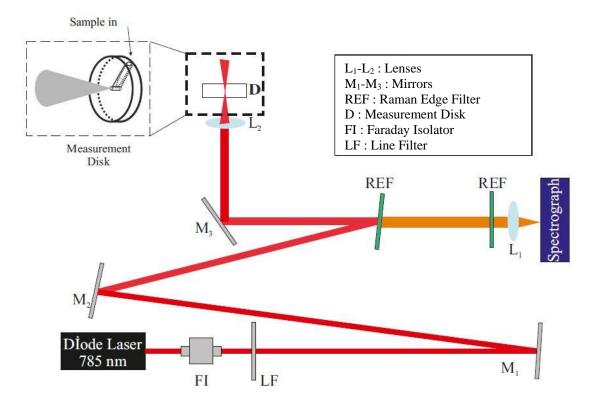
Figure 3.1 : Measurement setup for Raman spectroscopy of spent embryo cultures.

Raman edge filter reflects the photons whose wavelength are smaller than 790 nm and transmits the remaining portion. The normal of the REF was oriented at an angle of 6 degrees relative to the incident beam. This angle is the optimum value the operate in the lower Raman shift region by letting minimum laser photons transmit through the REF. This arrangement provides the minimum wavenumber of 160 cm^{-1}. Reflected light from the REF are sent to the objective lens (L$_2$) via a mirror M$_3$ to be focused on

the sample center. The collimated beam is reflected from REF providing the height of the beam matches the center of spectrometer slit, the beam is parallel to the ground, and vertical to spectrometer slit axis. The backscattered photons from the sample travel back following the same path of incident beam and they are filtered by the REF. The residual Rayleigh beams are dramatically decreased after the beam passes through the second REF. The transmitted light from this REF is imaged on the spectrograph (Andor Shamrock 303i) slit and then on the CCD camera (Andor DU-420). The spectrograph (a Czerny-Turner type) consists of two toroidal mirrors and a set of gratings on a motorized stage. The focal length of this system is 303 mm, and the aperture is f/4. The device has a wavelength resolution of 0.1 nm. The CCD camera is cooled to -90° to get rid of the dark noise.

Each sample was measured for 30 seconds with 20 repetitions. Since our diode laser's wavelength may change slightly during the operation because of ambient parameters like temperature and humidity. A toluene spectrum was measured before every measurement to have a reference to check laser stability and calibrate the Raman shift.

In the preprocess step, the spectra were first Raman shift calibrated using the calibration of toluene Raman spectra. The Raman shift calibration algorithm is summarized in the pseudocode in section 2.7.1.3.

After the application of this algorithm using our MATLAB code, the Raman shift calibrated spectra or the samples were calculated as given in figure 3.2.

After every measurement, a water spectrum was measured for background correction in the preprocess step. Although the water Raman measurements are quite similar, the measurement of these spectra were repeated after every measurement taking into account of the intensity instabilities in our laser. The water spectra corresponding to each measurement were subtracted and the background corrected spectra as displayed in figure 3.3 were obtained.
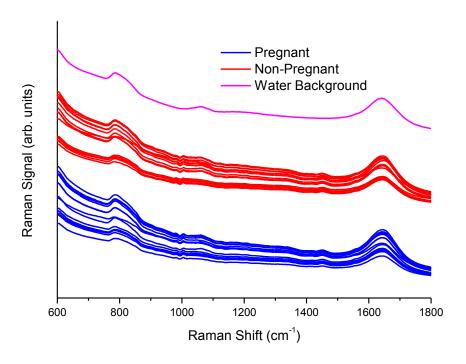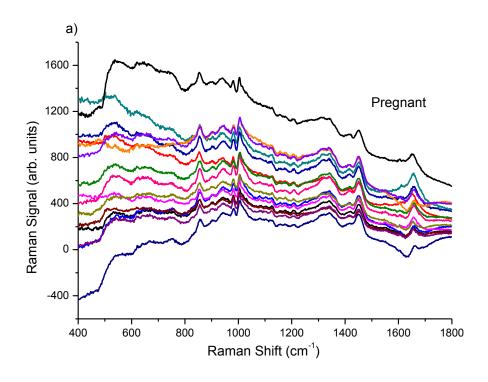
Figure 3.2 : Calibrated Raman spectra of raw embryo spent culture and water spectra. Non-pregnant group and water spectrum were shifted for better visual discrimination.

The background corrected spectra were baseline corrected and normalized. Baseline points were selected carefully in order not to affect the Raman peak intensities. The baseline point selection was realized in Grams AI software, which allows checking the peak position, by second derivative calculation. Besides, it applies real time baseline correction, which helps to see the effects of the baseline points on the spectrum. The baseline points were applied on every spectra (without updating their position) using the cubic spline algorithm in our preprocess code written in MATLAB. A vector normalization was applied on the spectra where all the data points are divided by the absolute norm of the data vector as given in the equation 2.76.

The baseline corrected and normalized spectra are displayed in figure 3.4. Groups are shifted in y-axis for better visual discrimination.
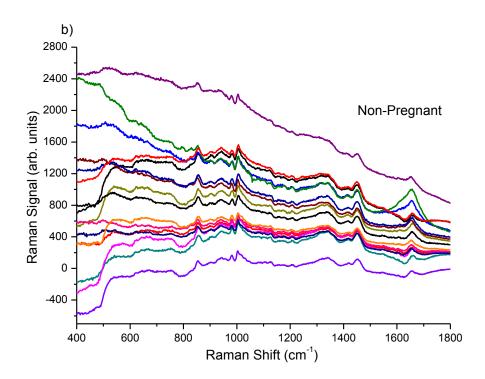
Figure 3.3 : Background corrected Raman spectra of embryo spent culture taken from the samples that a) could develop to pregnancy stage b) could not develop to pregnancy stage
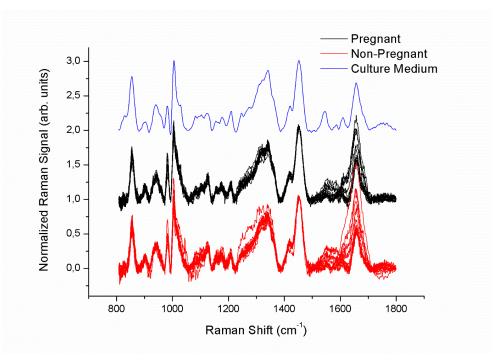
Figure 3.4 : Raman spectra of spent embryo culture samples (16 non-pregnant, 15 pregnant) and fresh embryo culture medium. Raman spectra of non-pregnant spent embryo culture samples and fresh embryo culture medium was shifted in y-axis for better visualization

Applying band component analysis on all these spectra, the band areas of all the peaks, whose positions were determined by second derivative analysis, were obtained using Grams AI 8 software. A Voigt profile was used during the analysis. A sample spectrum with fit components from each group is given in figure 3.5. In this figure, mean pregnant and non-pregnant spectra are obtained by averaging the spectra over all pregnant and non-pregnant measurements, respectively.
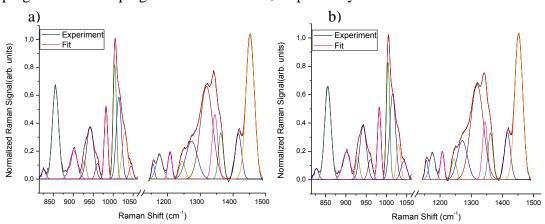
Figure 3.5 : Band component analysis of Raman spectra of mean a) pregnant b) non-pregnant samples. The regions of the analysis are 815-1065 cm^{-1} and 1140-1500 cm^{-1}.

A statistical test with Mann-Whitney U method was applied on the all band areas calculated and on the all the possible band area ratios. Using the most discriminatory band area ratio, which is 902 to 943 cm^{-1}, a K-means cluster analysis were performed to classify the spectra with an unsupervised method. Figure 3.6 demonstrates the scatter plot of the ratios.
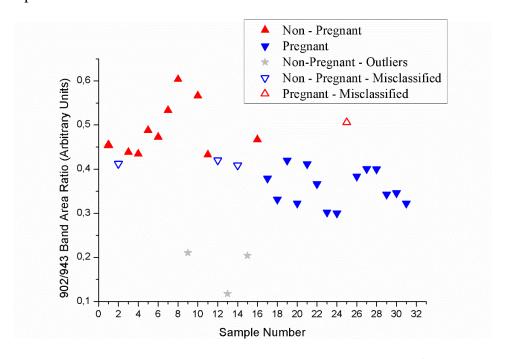
Figure 3.6 : The scatter plot of the band area ratios of 902 /943 cm^{-1} is shown. The upward triangular symbols represent actual non-pregnant samples, while the downward symbols represent the actual pregnant samples.

The points in the figure were colored due to their K-means indices. After the outlier analysis using the 2-sigma rule, three samples were found as outlier which were shown as stars in the figure. The sensitivity and specificity of this method was calculated to be 93% and 77%. The colleagues from medical school has assessed and graded the embryo using international embryo grading system (morphological assessment) [83]. They found sensitivity and specificity of 73% and 75%. These results were summarized in table 3.1 and table 3.2.

Table 3.1 : Classification performance of Raman spectra for spent embryo culture samples by means of band area ratios of 902 / 943 cm-1.

RAMAN	Pregnant Predicted	Non-Pregnant Predicted
Pregnant	14	1
Non-Pregnant*	3	10
Sensitivity	0.93	
Specificity	0.77	

Table 3.2 : Prediction rates for morphological assessment.

MORPHOLOGY	Grade I	Grade II or III
Pregnant	11	4
Non-Pregnant	4	12
Sensitivity	0.73	
Specificity	0.75	

Raman spectra of 14 amino acids in aqueous solution were also measured. These measured amino acids were phenylalanine, valine, glutamine, alanine, arginine, tyrosine, tryptophan, glycine, leucine, serine, histidine, proline, glutamate, and cysteine. Among these, the ones that contribute most to the significant bands were found to be glutamine, glycine, proline for 902 cm^{-1} and aspartic acid, and valine for 943 cm^{-1}. A comparison of the above-mentioned amino acids with mean spent culture spectrum is given in figure 3.7. It may be considered that glutamine, proline and glycine can affect the Raman intensity of 902 cm^{-1} band. In spite of the conflict in the literature that is about the effect of the individual amino acids on the embryo development, there is an agreement on the positive effect of glutamine and glycine on the embryo development [84-88]. Our study is consistent with these literatures.
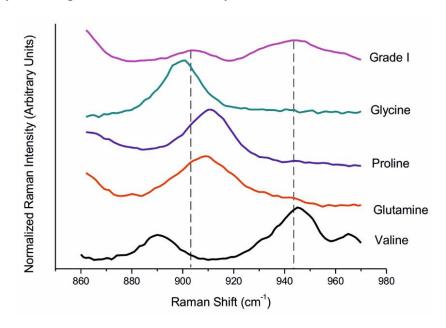

Figure 3.7 : The normalized Raman spectra of valine, glycine, proline, and glutamine and Raman spectrum of mean spent culture samples (pregnant) were overlaid in 860 – 970 cm^{-1} region. The normalized Raman intensity of mean spent culture samples was exaggerated and shifted in y-axis to increase visibility.

3.2 Sorting of Biological Particles with HORT Setup

Holographic Optical Raman Tweezers (HORT) is, as the name suggests, the combination of HOT and Raman spectroscopy. A HORT setup provides simultaneous evaluation of Raman spectrum acquisition from multiply trapped objects. These objects are automatically manipulated in the image plane individually to the predetermined Raman measurement positions. Signal is acquired from the individual trapped samples separately and is to be used for particle identification. Identified samples are also automatically moved to the desired positions where the streamline of the individual class is belongs.

3.2.1 Microfluidics Design and Production

The design of microfluidic channels is one of the most important step before getting to the production procedure. One first needs to understand the needs regarding to his/her application to decide the shape, diameter, length and other parameters of the channel.

Our channel is the most basic Y shaped channel which allows an inlet channel and two outlet channels with a circular chamber in the middle. This shape is decided as an initial design to experiment and see the drawbacks. However, it was not changed until the end of the study.

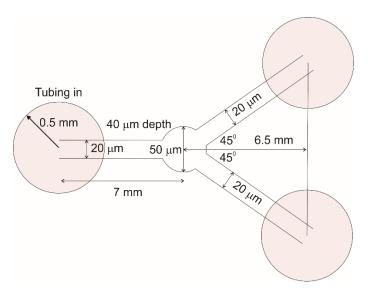The dimensions of the channel are given in figure 3.8:

Figure 3.8 : Dimensions of the Y-shaped microfluidic channel structure.

As seen in the figure, the channel width is 20 μm. This is suitable to flow single cells whose diameter generally between 5-10 μm. The diameter of the entrances of the

channels is 0.5 mm. This is designed according to the standard tubing adapter diameters. The chamber in the middle has a diameter of 50 μm. The depth of the channel is 40 μm. This was determined taking care of the Raman contributions from each interfaces of the chamber where one side is made of PDMS and the other side is glass. It was considered to find the minimum depth where the background signal from these interfaces does not bother the Raman signal from the trapped particle too much.

This design was drawn using Tanner L-Edit, which was licensed to ITU Nanotechnology Research Center. The redrawing was made by the group member Hatice Turhan (MSc student).

3.2.2 Procedure of Production

The procedure of PDMS channel production is a well-documented routine as given in literature section. This can be divided in three main parts: First, the production of the mask. Second, mold master fabrication using negative photoresist material such as SU-8. Third, production of PDMS channels by replica molding from photoresist masters. The production steps are summarized in the figure 3.9 below:

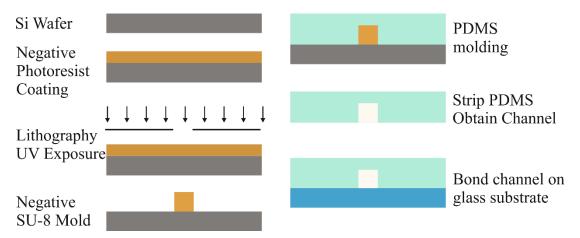**Figure 3.9 :** Fabrication steps of a microfluidic channel are shown graphically.

The chromium mask (photomask) was fabricated using a direct laser writing device which provides high resolution patterns.

After the fabrication of the mask, master molds made of SU-8 was made following the steps below:

- Clean the silicon wafer in three steps: Aceton – Isopropyl alcohol (IPA) – Deionized water (DI water).

53

- Coat the wafer with 4 mL SU-8 (100 mm diameter wafer) using a spin coater. The spin cycle times and the total spin times of coating is chosen from the producer's (Microchem Corp.) datasheet regarding the desired channel depth. In this study, it was 40 μm. Thus, the spin coating settings for this depth were 500-rpm spin for 5-10 sec with acceleration of 100 rpm/second and then 3000 rpm spin for 30 secs with acceleration of 300 rpm/second.

- Soft bake the coated wafer on a hot plate at 95°C. In our case, baking time is 15 minutes.

- Place the photomask on the soft baked photoresist and exposure it with Ultraviolet (UV) beam using a 250 mJ/cm^2 radiation during 10 seconds for 40 μm thickness. This will write the pattern of the mask on the wafer. A negative channel shape is formed.

- Apply post exposure bake (PEB) on the negative channel shape by heating at 65°C during one minute and immediately after that, it is baked at 95°C for 5min.

- The developer purchased from the producer (Microchem Corp.) is prepared in a petri dish and the baked photoresist is placed in the dish to be developed during 8 minutes for our applications. Wash the developed patterns with IPA and then dry them.

- Hard bake the photoresist at 180°C for 1.5 hours.

Following the master mold production process, PDMS elastomer is casted onto the produced mold. The procedure of PDMS replication is listed below:

- First, mix PDMS and the curing agent with 10:1 ratio to obtain the elastomer.

- Pour the mixture onto the wafer that includes the master mold. Remove the bubbles in a vacuum medium. Usually, 45 minutes is enough to get rid of all the bubbles.

- Hard bake the elastomer at 75°C for 2 hours in oven.

- Strip the PDMS layer and cut the individual chips. Punch holes.

- Plasma-bond the cover glass on PDMS using a plasma cleaner.

After the PDMS channel is produced in the clean room facility following the steps above, three holes were drilled on the microscope slides to fit the tubing inlets in the PDMS channels. Then the channels were adhered on the slide using Entellan™. These steps of the procedure are specific for our application.

3.2.3 Construction of HOT Setup & Multiple Trapping

The experimental setup in figure 3.10 was built in order to realize multiple trapping and Raman spectra acquisition.
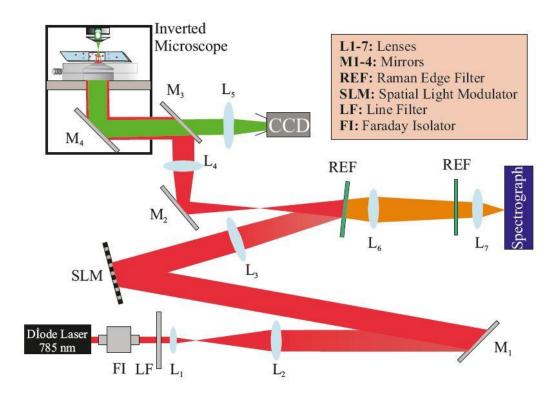
Figure 3.10 : HORT setup built in Istanbul Technical University.

This setup was built in the Laser Spectroscopy Laboratory in Istanbul Technical University Physics Engineering Department. The laser source is a diode laser with a wavelength of 785 nm and a power of 100 mW. The beam in the output of the laser passes through Faraday isolator and laser line filter and is expanded to fulfill the active area of the SLM by a Keplerian telescope system which has two lenses (L_1 and L_2) with focal lengths of $f_1 = 45$ mm and $f_2 = 200$ mm.

The polarization of the laser is horizontal after the transmission from Faraday Isolator, which is desired for SLM illumination. The reflected light from the SLM steers the incident beam to the REF. The REF reflects the beam with a wavelength less than 785 nm via M_2, M_3, and M_4 mirror. L_3 and L_4 lenses were located in the 4-f configuration.

These lenses image the computer generated hologram displayed on the SLM on the BFP of the microscope objective. The microscope objective is water immersion type (Olympus UPLSAPO 60XW) with numerical aperture of 1.2 and magnification of 60X.

All high order beams and zeroth order beams are targeted in the sample plane. Among these, the first order beams are the most prominent ones because of the hologram algorithm that is used as can be seen in figure 3.11. In this image, five spots are created in the image plane and the hot spots in the picture are the reflections of the created spots from the cover glass. The relatively weak spot in the middle is the zeroth diffraction order from the SLM. The background corrected image is given in 3.11-b in order to compare the light intensities of the first order beam and the zeroth order beam easier.

The higher order beams are also present in the image plane since they were not blocked, however, their power is very small comparing to the first order spots, and they do not have the ability to trap.
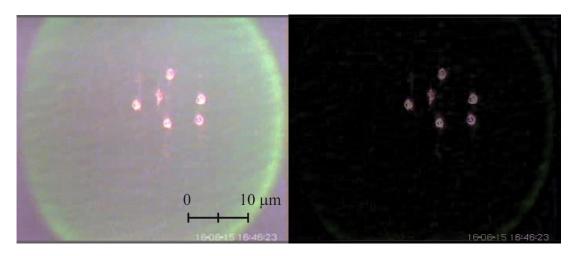
Figure 3.11 : a) Five spots are placed around zeroth order spot. b) Background corrected image of (a) to compare spot intensities better.

The backscattered and back-reflected beams follow the same path with the light coupling into the microscope objective. A portion of the beam is reflected and the remaining is transmitted. The REF transmits the inelastically scattered Stokes beams and the Rayleigh beam whose wavelength is larger than 785 nm. In summary, the Raman spectra are collected with a 180° geometry setup.

The scattered light is collected with a lens L_6 and focused onto the entrance slit of the spectrograph using a lens L_7 with focal length of 45 mm. In a Full Vertical Binning

(FVB) scheme, the signal in each column of CCD is summed to obtain a single spectrum from the whole detector area. However, in a Multi-Track (MT) scheme, the CCD can be binned to several tracks to obtain individual spectra from each tracks as in figure 3.12. In this figure, since the PS particle in the second track is not well located in the column of monochromator slit, the signal is weaker.

Figure 3.12 : Multi-track Raman acquisition.

This means moving a spot laterally using HOT will dramatically decrease the Raman intensity. In other words, the intensity will drop fast in horizontal movement. That gener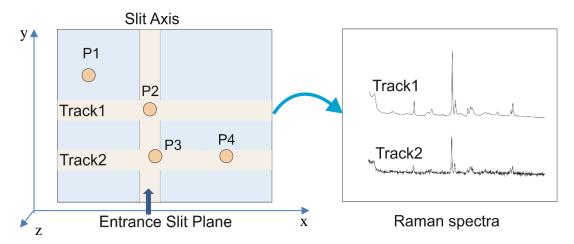ally allows one to obtain Raman spectrum of only one particle at a time. In the direction of y-axis, the beams originating from the spots in the sample plane are incident on the slit normal with an angle. They are not parallel to the optical axis. Considering this, it is expected the spots away from the slit center to provide lesser Raman signal. Therefore, it is a challenging task to obtain spectra of multiple particles in different positions or of a 2-D array.

In the study, PS particles whose diameter is 4,5 µm were trapped. The solutions including the PS particles were prepared with a low concentration to obtain isolated trapped particles. This solution is sampled in a glass measurement cell, which was prepared by drilling a glass microscope slide a hole whose diameter is 10 mm. Although the depth of the measurement cell is 1 mm, the working distance of the microscope objective is 280 µm. Therefore, the traps can be created at a maximal distance of 280 µm in the measurement cell. In this measurement cell, a four-spot array was created and manipulated to the Raman measurement region. Binning the CCD pixels in four tracks, Raman signal from the trapped particles could be collected, individually. The simultaneously obtained trap image and multi-track Raman image are given together in figure 3.13.
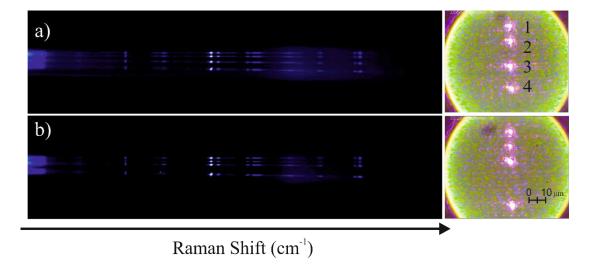
Figure 3.13 : Two Raman images obtained from the multiply trapped PS particles seen in the right side of the images. The particle number four was moved downside and number three was moved upside before the measurement of the image in (b).

The experiments were proceeded in Istanbul University Laser Spectroscopy Laboratory in the Atomic and Molecular Physics Department administrated by Prof. Dr. Gönül Başar. The reason of changing the location is that the new laboratory has a high power laser source that could enable high number of traps.
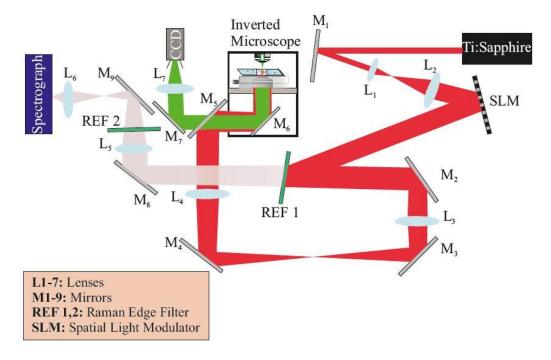
Figure 3.14 : HORT setup built in Istanbul University.

Figure 3.14 shows the experimental setup built in this laboratory. In this setup, a tunable Ti − Sapphire laser (Coherent MBR ring series, 700 − 1030 nm) which is pumped with a DPSS laser (Coherent Verdi) were used. Output power of the laser was

58

decreased from 4 W to 2 W using a 50/50 beam splitter. The laser power used in the experiments is about 900 mW. The wavelength was adjusted around 782 nm. The beam is expanded using a Keplerian telescope system as always used in our optical tweezers setups. This expanded beam is used to illuminate SLM display fully. The polarization of the laser is horizontal which is desired for SLM illumination. The reflected light from the SLM is directed to the Raman Edge Filter (REF), which reflects wavelength less than 790 nm. The reflected beam passes through the L_3 lens, which is one element of the 4-f configuration together with L_4 lens. The beam is directed into the microscope objective's back aperture via dielectric mirrors M_2-M_6. As in the scheme in the previous setup, the backscattered light follows the same path and is collected after it transmits from the two REFs using an objective lens. An optional lens (L_5) was used to optimize image magnification.

Figure 3.15 shows the optimization steps of the Raman images that were improved by adding a collective lens (L_5) behind the second REF and changing its focal length to 500 mm from 750 mm. The test particles, PS particles, have a 4,5 μm diameter. They are assembled vertically in the Raman measurement region in a glass measurement cell. The measurements in figure 3.15 were obtained with 10 seconds exposure time. In the first image, 3.15-a, the measurement was obtained without the L_5 lens. The figure shows that the Raman image is not resolved well spatially for four traps. This image is improved by optimizing the optical path by adjusting the steering mirror M_9. This let us obtain a better image as displayed in figure 3.15-b. To correct the divergence in the image, a collecting lens with a focal length of 750 mm was adapted behind the second REF which let us obtain the image in figure 3.15-c. As seen in this image, divergence was improved but it did not totally disappear. This lens was replaced with one whose focal length is 500 mm. The image was improved and show better spatial resolution compared to the other images as seen in figure 3.15-d. The Raman measurements were taken from trapped particles at a depth of 10 μm in (a) and (b), and 30 μm in (c) and (d). The Raman spectral images are not parallel in all four images as seen in figure 3.15. This stems partly from the imaging errors of the spectrograph. Additionally, the light coupling into the spectrograph may not be perfect.

The multi-track Raman spectra of the trapped particles whose Raman images are shown in figure 3.15 were also measured. These spectra are shown in figure 3.16. The images of the trapped PS particles in the MO object plane are given in the inset of each

image. The exposure times of the measurements are one second except the one in 3.16-a. In that measurement, the exposure time was set to ten seconds.

Raman Shift (cm^{-1})
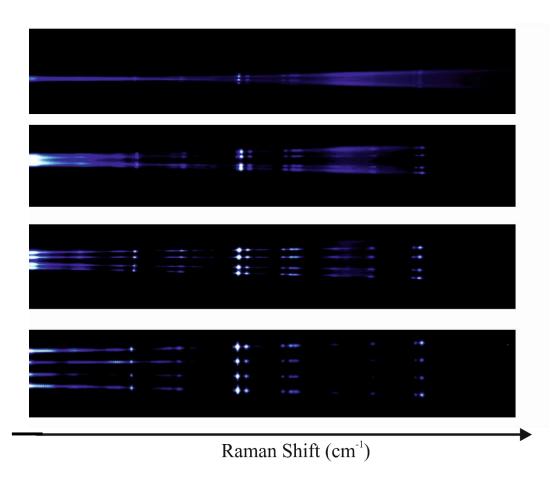
Figure 3.15 : Raman images from four PS particles with three different configurations a) No collecting lens is used after REF 2. b) The optical elements were adjusted to obtain a better image. c) A 750 mm lens is used. d) A 500 mm lens is used. All measurements are done with 10 seconds exposure time with imaging scheme of Andor software.

As can be seen, the image acquired from the camera that displays the MO image plane is improved with the help of a colored bandpass filter (BG 38, Newport). This filter blocks the beam with wavelength between 730 and 1150 nm with a reflectivity coefficient larger than 90% and transmits the beam between 350 and 600 nm with at least 90% transmission coefficient. This filter rejects the unwanted back reflected or backscattered light from the sample and the interference patterns created by the SLM. It must be noted that the wide peaks around 1300-1400 cm^{-1} stem from the fluorescence signal from the cover glass since the measurement was taken with the particles very close to the surface of the cover glass.

Since, the measurement was taken 30 μm above the cover glass, the contributions from the cover glass was very weak for figure 3.16-c and d while it is larger for the spectra shown in figure 3.16-a and b.
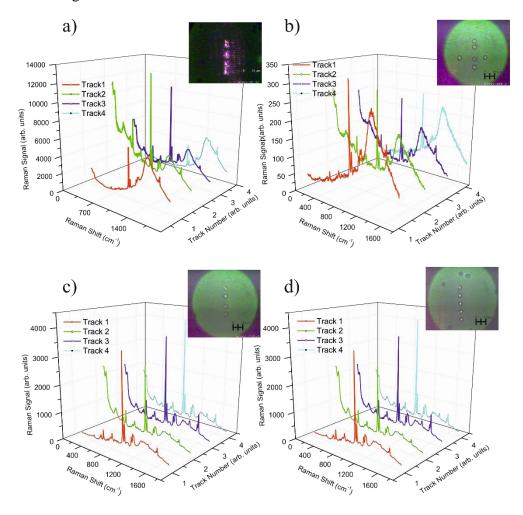
Figure 3.16 : Multi-track Raman measurement obtained from the PS particles in shown in the insets. Four PS particles are in Raman region in all four images. Measurement was done with the exposure time of a) 10 seconds, b-d) 1 second. The fifth particle in lower side of the (d) image is trapped by a ghost spot.

The lower trap in figure 3.16-d inset is a ghost trap and it did not display any signal neither in the Raman image, nor in the multi-track spectra. The reason why there is no signal from the ghost trap is that the beams scattered from the image of that particle is constructed outside the spectrometer slit. In figure 3.16-d, the particles assembled with equal distances provided by the HOT software. The edge-to-edge distance of the PS particles are calculated to be 2.5 μm, which was obtained by image processing of the image in the inset of figure 3.16-d. However, it is shown in the inset of figure 3.16-b that the closest edge-to-edge distance the Raman spectra are spatially resolved is ~1.2

µm. Besides, in figure 3.16-d, five particles are in the trap in contrary to other images where there are four trapped particles.

To demonstrate the power distribution on the spots, the power on each spot in the Fourier plane was measured. The powers of these spots were measured on the focal plane of lens L$_3$. In the measurement, there were six spots, two of which were ghost spots. The results are shown in table 3.3. The laser power was adjusted to 700 mW before this measurement. Considering that the SLM has an average loss of 50%, the power in the Fourier plane distributed to these six spots is 310 mW. This power was not evenly distributed on the spots as can be seen in the table. Reason for this is that the computed intensity distribution may not match with the real distribution in grating and lenses algorithm since it only takes the phase part of the field into account. Considering that the Raman spectral intensity is directly proportional to the power, this distribution is obtained for the Raman intensity measurement of the particles, too.

Table 3.3 : Power distribution on spots in figure 3.15-d.

Spot #	Power (mW)
Ghost	27
1	67
2	44
3	50
4	103
Ghost	20
Incident Power= 700 mW	

The Raman image of 1003 cm^{-1} band of PS from figure 3.16-d was fitted with Lorentz line profile. The average full width at half maximum of the peaks was calculated along the vertical direction and was found to be 2,64 pixels as shown in Fig 3.17. Having known the pixel pitch of the CCD camera is 26 µm, each spot has the average image size of about 68,6 µm. The spot diameter at the object plane of the MO can be calculated with the equation 3.1.

$$D = 1.22 \, x \, \frac{\lambda}{NA} \tag{3.1}$$

Where λ is the wavelength of the beam to be focused from objective lens, D is the diameter of the spot in the focus of the lens, NA is the numerical aperture of the lens.

This value is 1.20 for the microscope objective in the setup. Thus, the spot diameter in microscope sample is 798 nm. The magnification is, therefore, calculated to be 86.

After a lens with a smaller focal length was used to obtain figure 3.15-d, the image size was inreased as seen in the figure. To calculate the image size on CCD image plane and the magnification, a Lorentz fit was applied on this image as in figure 3.18.
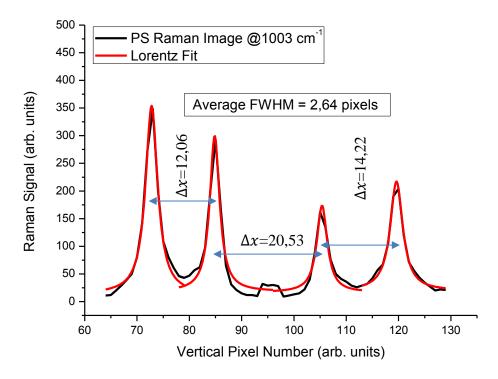

Figure 3.17 : Lorentz fit for the intensity distribution around 1003 cm^{-1} band of PS Raman image in figure 3.15-c. FWHM = 2,64 pixels.
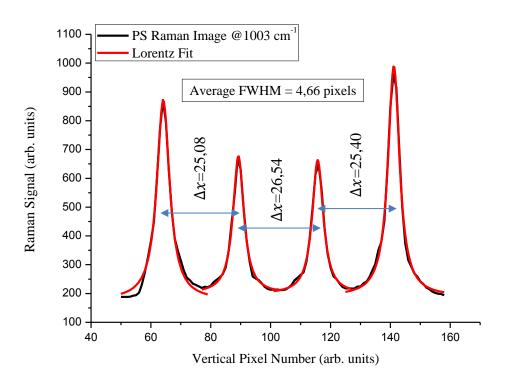
Figure 3.18 : Lorentz fit for the intensity distribution around 1003 cm^{-1} band of PS Raman image in figure 3.15-d. Average FWHM is 4,66 pixels

According to the calculation the average image size is 26 x 4,66 = 121 µm. The new magnification value is 121/0,798 = 152. When figure 3.17 and 3.18 are compared, the distances between the band centers are expanded as the magnification is increased which is expected and consistent with the images in figure 3.15-c and 3.15-d. The distance between peak centers are 25.7 pixels in figure 3.18.

Measurements in the PDMS microfluidic channel were performed using both ITU and IU setups. PDMS is a Raman active material that has very sharp and intense peaks in the low Raman shift region. A Raman measurement of PDMS and a PS are displayed overlaid in figure 3.19. These measurements were taken with one-second exposure time. Raman spectra of PS particles were measured at an equal distance of 20 µm from both surfaces where the surface materials are PDMS in the upper side and cover glass in the lower side. Although the Raman spectrum of PS was obtained in the microfluidic channel, there is no contribution from PDMS Raman bands. As seen in the figure many of these peaks are not overlapped.
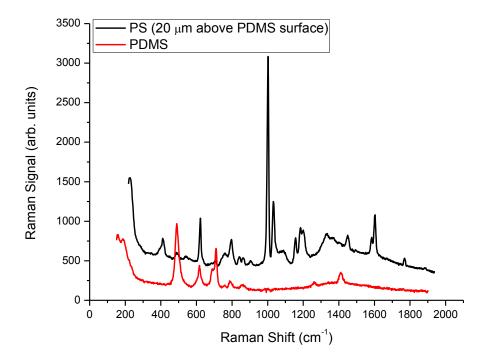

Figure 3.19 : Raman spectra of PS and PDMS are overlaid for comparison.

During the study, several alternative methods for pumping were tried such as a use of peristaltic pump or driving the syringe with a micrometer. These attempts did not result

in a uniform flow and desired flow velocity. Despite an unstable flow in the channel, three PS particles could be trapped as seen in figure 3.20. There are four spots in the figure, three of which have PS particles trapped. The Raman image of this array is displayed in the same figure, too. The signal from particle 1 could not be visible clearly in the Raman image. The signal intensity could be higher if the trap location was a little above its position in the same plane. The distance between two close traps in the figure is 1.65 μm.
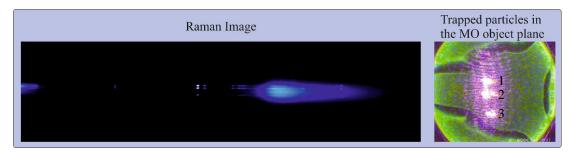
Figure 3.20 : Three PS particles trapped in a four-spot array in a Y-shaped PDMS microfluidic channel at a depth of 10 μm.

The microfluidics experiments could not be continued. It was observed in the experiments that the flow was not stable when the outlet tubings are left open without connecting to a syringe.

3.2.4 HORT for Biological Cells

After the tests with PS particles, biological cells were measured with the HORT setup. Yeast and E. coli cells were chosen for measurement. ITU Molecular Biology and Genetics department produced these samples for us before the measurement day. Zeynep Petek Çakar's group has prepared the yeast cells and Deniz Şahin has prepared the E. coli samples.

Both E. coli and yeast cells are cultured in the phosphate buffer saline (PBS) solution. These samples were measured in their own medium after diluting 100 times. Measurements were performed with four spots in the Raman region. Raman spectra of trapped E. coli and its medium PBS are shown in figure 3.21 together with PBS corrected spectrum, overlaid. These measurements were performed for 30 seconds exposure time with full vertical binning (FVB) scheme. The PBS subtracted spectrum is multiplied by two for a better vision.

The Raman measurement of a yeast cell is given in figure 3.22 overlaid with PBS and PBS corrected spectra. The spectra have some sharp peaks, which arises from the ambient light. Considering that the PBS spectra also have these contributions, when subtracted PBS background spectrum, the measurements will be free of these spikes.
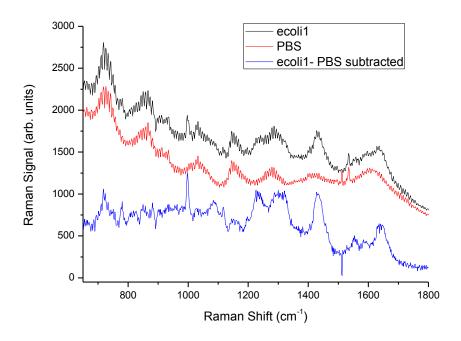

Figure 3.21 : Raman spectra of E. coli, PBS medium, and PBS subtracted E. coli. The PBS corrected spectrum was multiplied by two for better visualization.
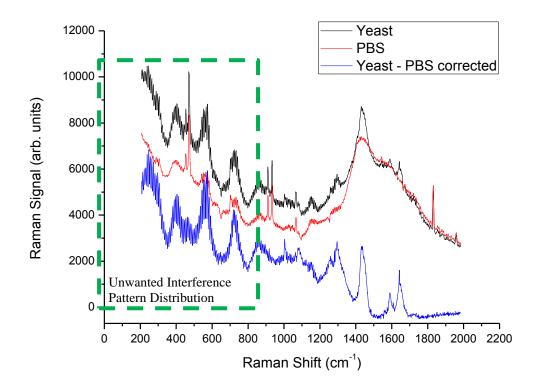
Figure 3.22 : Raman spectra of yeast cell, PBS medium and PBS subtracted E. coli. The PBS corrected spectrum was multiplied by two for better visualization.

There are some ripples in the low Raman shift region of the spectra. One reason causing this maybe the interference patterns generated by the computer generated hologram displayed on the SLM. Another possible reason is the use of a thick plane parallel mirror This unwanted pattern is broad and covers the Raman signal in that spectral region. Thus, the identification of the spectra will be made by neglecting this spectral region until 1000 cm^{-1} and taking into account of the upper Raman shift region. A comparison of the Raman spectra of yeast cell measured using conventional optical tweezers setup and holographic optical tweezers setup is displayed in figure 3.23. The ripples in low Raman shift region are absent in the measurement taken with conventional setup.
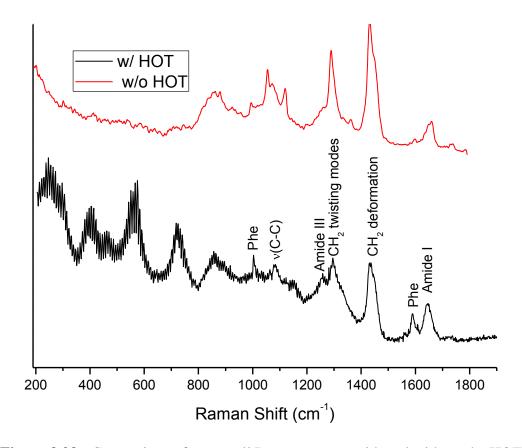
Figure 3.23 : Comparison of yeast cell Raman spectra with and without the HOT setup. The cells are trapped with conventional optical tweezers setup that does not use an SLM in the measurements without HOT. Band assignments are labeled on the peaks [89].

The band assignments related to yeast spectra are given in this figure, too. The bands at 1003, 1257, 1602 and 1650 cm-1 protein related bands. The bands at 1257 and 1650 cm-1 are assigned to amide I and III, respectively. These bands are used to extract

secondary structure of the proteins in the sample. The bands around 1100 cm-1 are related to C-C streching vibrations. The band at 1440 cm-1 is assigned to CH2 deformation the band is present in lipids and proteins. 1602 cm-1 band was shown to give sign of yeast cell's viability [81]. The band at 1003 cm-1 is assigned to ring breathing of benzene for Phenylalanine.

3.2.5 Classification of Trapped Objects Due to Their Raman Spectra

To make Raman based classification with the trapped particles; few classification algorithms were developed and tested. Since our model study was to discriminate PS from a certain biological cell, the methods below were used:

- PCA based identification

- 1003 band comparison

- Correlation coefficient comparison

3.2.5.1 PCA based identification:

A MATLAB code to classify spectra using PCA algorithm was written to use real time particle identification. This code needs a training dataset and a test measurement as inputs and gives a classification vector as output, whose elements are integer numbers between 0 and 2 when classifying two kinds of objects. The training dataset was first prepared which consists of normalized and calibrated Raman spectra of yeast cells and PS particles. The test measurements are obtained real time and the software appends them to the dataset to form the expanded dataset. A sample measurement is shown in figure 3.24. PCA is applied on this expanded dataset to find the scores and loadings. The distances between the scores give a measure of clustering of the measurements.

To determine the confidence limits of the clusters, an error ellipse is calculated by taking into account of the calculated distances excluding the test measurements. This ellipse is drawn onto the scores plot as in figure 3.25. The confidence limit while calculating the ellipse function in this study was chosen to be 99%, which is provided by three-sigma standard deviation. The classification of the measurements is made by determining which ellipsoidal limits the scores representing the measurements are within.

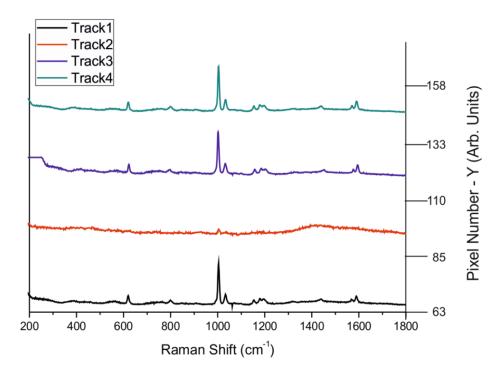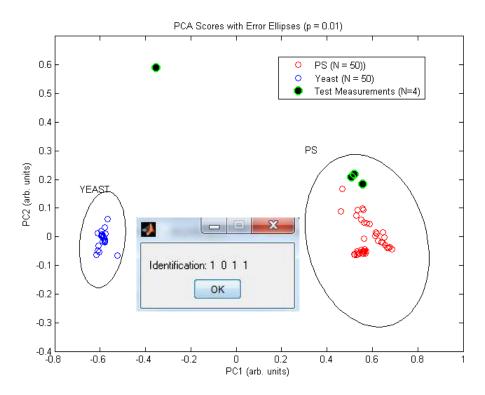**Figure 3.24 :** A multi-track PS measurement. There is no signal in track 2.

Figure 3.25 : PCA scores graph that includes the error ellipse calculated from distances of the groups. PCA scores of test particles are overlaid with error prediction graph measured for the dataset. For a multi-track Raman measurement of PS test particles, software gives the [1 0 1 1] output which is consistent with the measured particle.

When the test measurements are plotted overlaid with this graph as in figure 3.25, it becomes clear which class the measurements take place with human vision. To automate this process, rather than human vision, a few code lines are added to understand which ellipse the individual measurements are in. For example, if the task is to separate PS from yeast cell, program outputs "1" for PS and "2" for yeast cells. If the measurements are in none of the ellipses, they are unclassified. The output from the identification function is the state vector whose elements are integers between zero and two. Identified particles are manipulated regarding to this input.

3.2.5.2 Comparison of peak at 1003 cm^{-1}

Identification using 1003 cm^{-1} band is quite straightforward. This is the marker band of PS and it is most intense peak. This peak is present in some of the biological molecules, too. However, Raman spectra of microorganisms do not include a sharp and intense 1003 band. This enables one to define certain threshold limits to identify certain spectra. Our problem is, in the simplest case, identify PS and yeast particles to label them '1' and '2'. If the measurement can not be classified, label is '0'. The cut-off value to classify PS and yeast measurements were found by analyzing the previous measurements. In summary,

$$Identification: \begin{cases} 1 & if\ Th \geq 0.85 \\ 2 & if\ 0{,}2 < Th < 0{,}8 \\ & else \quad 0 \end{cases}$$

BSc student Neşe Didem Temeltaş has implemented the code during her Advanced Physics Project. She applied it for PS, yeast cell and mixed solutions. The algorithm worked with a 100% success. However, this approach was not followed because the algorithm should be more general and be useful for every measurement. This method is useful when investigating the spectra that can be sorted by the peak at 1003 cm^{-1}. This applies for PS particles and yeast cells; however, this is not a general case. One may want to classify spectra other than PS or yeast cells. In this situation, he/she should define the discriminative band, the threshold and then write the code lines for these.

3.2.5.3 Correlation coefficient comparison:

Correlation coefficient is a measure that defines how similar two measurements are. This coefficient is defined with the equation 3.3 below [90]:

$$r = \frac{n\sum xy - \left(\sum x\right)\left(\sum y\right)}{\sqrt{n\left(\sum x^2\right) - \left(\sum x\right)^2}\sqrt{n\left(\sum y^2\right) - \left(\sum y\right)^2}}$$

(3.3)

In this equation r is the correlation coefficient, n is number samples, x and y are the measurements. The use of correlation coefficient comparison is founded on very similar principles as the PCA based algorithm. This algorithm compares the correlation coefficient of the database matrix with the test measurement. The correlation coefficient vector of a sample measurement with respect to the dataset is plotted in figure 3.26. In this figure, the correlation coefficient of a PS measurement with each dataset measurements is shown.
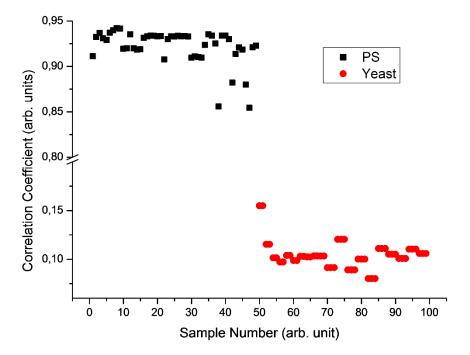

Figure 3.26 : Correlation coefficient vector of a sample measurement with respect to the dataset is plotted.

The main parameters of this figure are summarized in table 3.4. It can be seen that the correlation coefficient of the sample PS measurement with the PS measurements in the dataset matrix are not smaller than 0,85. The coefficient is not greater than 0,16 for the yeast cells.

71

Table 3.4 : Summary of the correlation coefficient calculation.

Average Correlation Coefficient			
With PS	**Tolerance**	**With Yeast**	**Tolerance**
0,92	± 0,019	0,10	± 0,014
Extreme Points			
Min	**Max**	**Min**	**Max**
0,85	0,94	0,080	0,16

With this pre-calculation, one could empirically define safe limits for the identification:

$$For\ each\ kind\ of\ spectrum: \begin{cases} define\ 1\ if\ c_i \geq 0.85 \\ else, \\ define\ 0 \end{cases}$$

Since correlation coefficient algorithm is 1.3 seconds faster than the PCA algorithm (calculated by measuring the CPU times while running the codes) and does not need modification according to the application, this algorithm was chosen in the experiments.

3.2.6 Sorting Experiments

A model classification study was designed in this study to test the classification algorithms and the HORT setup. Raman based sorting experiments were performed with the optically trapped yeast and colloidal PS particles (Polyscience, 4.6 ± 0.27 µm) in liquid medium. A computer program has defined trajectories for the particles to be manipulated using pre-calculated holograms.

The PS sample was prepared from the liquid solution diluting a drop of sample with 1 mL of distilled water. This solution was dilution 100 times to obtain stable and isolated traps that are not disturbed from neighboring particles. Yeast cells are received in PBS solutions. This solution is very dense of yeast cells. 1 mL from this solution was taken and it was diluted 100 times with PBS. These two diluted PS and yeast cell solutions are mixed equally. 120 μL of mixture were poured into the glass measurement cell covered with microscope slide.

A sequence of pictures from the sorting experiment with this solution is shown in figure 3.27. There are eight traps located at predetermined positions on plane as emphasized with red circles in Fig. 3.27a. The depth of these traps is about 20 µm. Some particles were trapped at different positions other than the predetermined trap

positions. The traps appear at these positions are called ghost traps (see explanation in section 2.3.2.4). These ghost traps were indicated with stars in Fig.3.27a. Four of eight particles on the right column of traps were located in the Raman measurement position. There is no particle in one of these four traps. Our software measures the Raman spectra of these four-spot array and applies the identification algorithm to label them as "1", "2" or "0". The algorithm labels PS as "1", yeast cells as "2" and unknown spectra as "0" according to the spectra displayed in figure 3.28. The spectra in 3.28 were obtained with one-second exposure time using multi-track binning scheme. The spectra were measured by our software and saved after subtracting the background measurement, which was obtained without particle in the traps. The input for the classification software is the uncalibrated raw spectrum, as shown in figure 3.28.

The classification software first calibrates the spectra using the calibration data of the PS spectrum measured initially. Then, a baseline correction is applied on the spectra to reduce residual background, which stems from fluorescence and unwanted scatterings from optics. Finally, the spectra are normalized relative to their maximum intensity. Since the spectra are measured with one-second exposure time and they usually have a noise profile, the normalized spectra are smoothed with Savitzsky-Golay smoothing procedure. n figure 3.28, there are spectra measured from PS, yeast and background. Since the spectra are background corrected, there is no signal from the trap 2 point with no trapped particles in it. The yeast spectra in Track 3 and Track 4 are broad, however after a baseline correction; the software calculates a correlation coefficient that is enough to determine them as yeast cells as seen in figure 3.29. The peaks at 1300, 1440, 1602 and 1650 cm^{-1} are apparent after this operation. These bands are absent or present with low intensity in PS spectra.

The classified particles have certain positions to be targeted. The regions including these positions are shown with two boxes in figure 3.27-e assigned with Gr1 and Gr2. The image shows us that the particle in the upper side of the array is classified as "1" since it is manipulated towards the upper corner of the frame (figure 3.27a-d). Notice that the particle at the top of the trap line moves together with the ghost trap. While this particle is manipulated, other particles labelled with "2" or "0" holds their position to maintain the traffic stability. After the PS particles labelled as "1" have finished their travel to upper corner, yeast cells are targeted to the lower corner (figure 3.27e-h). After the particles with label '2' starts their motion, the second four-trap array moves to the measurement position, simultaneously (figure 3.27e-h).
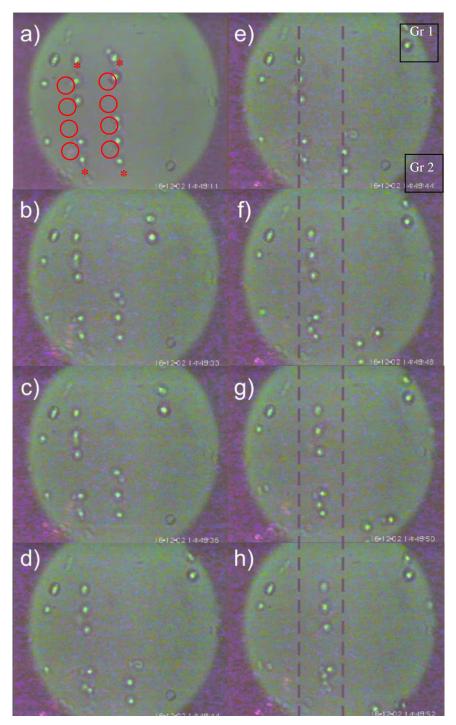
Figure 3.27 : Sorting with PS and yeast cells. The program moves the array to the measurement position. After the investigation of the data, particles are classified and then they are manipulated to the final positions. In the picture a-d) PS is labeled as "1" and manipulated to upper corner of the chamber. e-h) the yeast cells located in the lower side of the array are labeled as "2" and manipulated towards the lower corner of the chamber. The dashed lines are inserted to follow the particle movement.
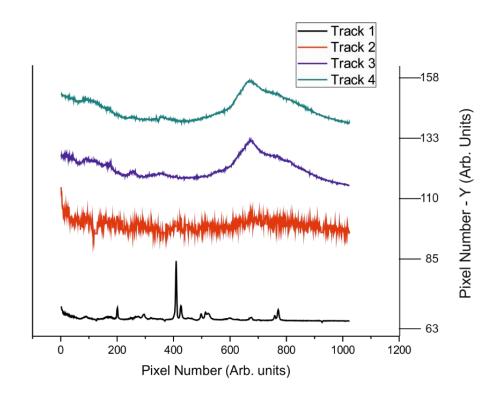
Figure 3.28 : Raman spectra from the trapped PS particle and yeast cells.
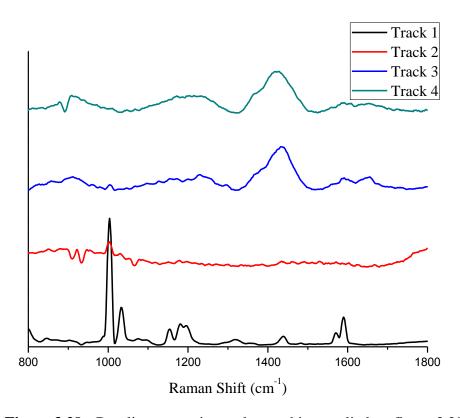
Figure 3.29 : Baseline correction and smoothing applied on figure 3.28.

The power of the ghost traps may dramatically change when the spatial position of the spots change. As discussed in [41], the superposition algorithm distributes some portion of the power to ghosts.
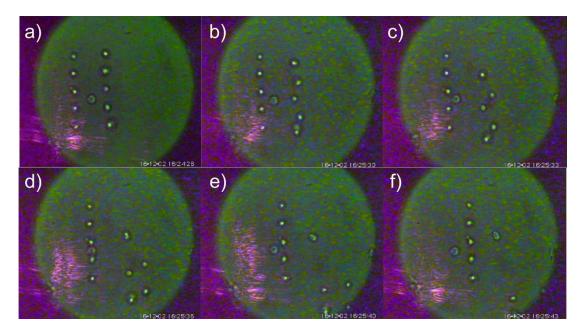
Figure 3.30 : Automatic manipulation of the same type of particles.

Above in figure 3.30, the classification and manipulation of the same type of particles is demonstrated. Five yeast cells were trapped in the mixed solution described above. There are four other particles in the other group holding in the line to be measured after the first four. Figure 3.31 shows the measurement obtained from four particles on the right array in figure 3.30 a simultaneously. The spectra in the figure indicate that all four particles are same. The software detects this after an automatic baseline correction and normalization as shown in figure 3.32. The identification of all four particles are made using these preprocessed spectra. In this sample measurement, the software finds the class of all four measurements the same and labels them as yeast cells with label "2".
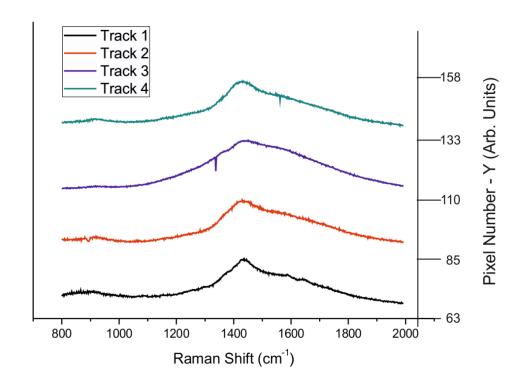
Figure 3.31 : Input Raman measurement for the classification of the particles in figure 3.30.
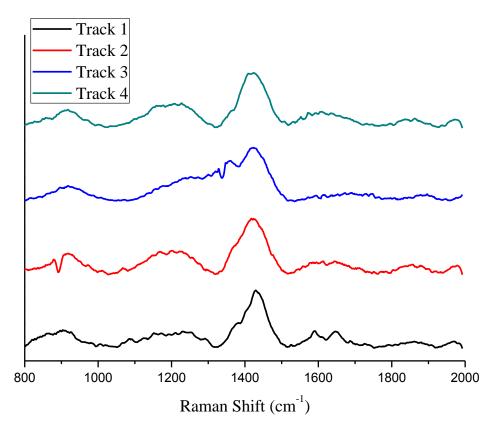
Figure 3.32 : Baseline corrected Raman spectrum for figure 3.31.

77

4. CONCLUSION

This study aims to sort biological cells, which are immobilized in a microfluidic channel by holographic optical tweezers, according to their chemical signals obtained by Raman spectroscopy. To do this, a HOT setup have been constructed first in Istanbul Technical University and then in Istanbul University. The study continued in the latter one because a higher laser power was needed to trap and manipulate more particles, stably. The multiple trapping with test particles was achieved in both setups seen in figure 3.13 and figures 3.15-16.

Although the initial plan was to do the sorting in a microfluidic channel, the test experiments in the microfluidic channel has failed since a proper syringe pump was absent. Instead, the sorting experiments went on in a home-made glass measurement cell.

Sorting experiments were done with PS particles and yeast cells. A signal taken from E. coli cells with 30 seconds exposure time is given in figure 3.21. E. coli cells were not used in the sorting experiments because long exposure time acquisition was needed to collect significant signal. On the other hand, figure 3.28 show that an exposure time of one second gives enough signal for the classification of the yeast cells.

The CPU time spent for the classification of four particles using the PCA based algorithm is 1.3 seconds more than the one spent in correlation coefficient approach (0.8 s and 2.1 s). This is why the PCA based approach was not chosen in this study. Moreover, the algorithm that compares the band intensities at 1003 cm^{-1} was not used, either. This algorithm needed a generalization since the classification criterion is specific to the current problem, which is classifying PS particles and yeast cells. Correlation coefficient approach was used in the study since it proved to be faster and more general.

The adjustment of the thresholds in correlation coefficient approach was made by calculating the correlation coefficients of a test measurement with the measurements in the dataset. The result of this calculation, as given in figure 3.26 and table 3.5 gave

the threshold values that the software needed as inputs. This algorithm gave accurate results for the classification of the spectra PS particles and yeast cells. Using this classification output as an input, the task to manipulate particles to the target real-time was achieved by the HOT software.

Sorting due to Raman signal has its own limitations, too. The main challenge in the sorting experiments is the speed, which is the sorted cell number in unit time. However, biological cells generally give weak Raman signal. Unless one uses resonance methods, one second or less exposure times may not be enough for acquiring a Raman spectrum that can be identified. Moreover, long exposure times make the sorting inefficient. There will be further efforts to overcome this challenge in the future experiments. The first thing to try at this stage is to make traffic optimization of the trapped particles move faster and thereby allow more particles to be separated at the unit time.

The hologram algorithm used in this study is gratings and lenses algorithm. As mentioned in the experiments part, this algorithm causes non-uniform power distribution and undesirable ghost spots, which reduces the power of generated spots irregularly. In the literature section, it was mentioned that the GSW algorithm proved to be extremely uniform and efficient. Our next goal after this thesis is to implement this algorithm into our software to obtain a better power distribution, free of ghosts. Besides, this algorithm supposedly allows us to obtain a lesser intensity for zeroth diffraction order.

During the PhD study, the assessment of embryo quality using the Raman spectra of the spent embryo culture media has been studied. The hypothesis was that the embryo that nurtures well consumes the certain amino acids more than the other ones. Our study showed that there is a significant difference in the band area ratios of 903 / 942 cm^{-1} as seen in the figure 3.6 and table 3.1 and 3.2. According to our Raman measurements with amino acids, four amino acids have strong bands that could contribute to this weak signal. These are glutamine, glycine and proline for 903 cm^{-1} band, valine for 942 cm^{-1} band. These results have a positive correlation with the literature especially for glutamine and glycine where there is consensus on their positive effect for the embryo development.

REFERENCES

[1] **H.M. Davey**, **D.B. Kell**, (1996). Flow cytometry and cell sorting of heterogeneous microbial populations: the importance of single-cell analyses, *Microbiological reviews, 60,* 641-696.

[2] **Y. Xia**, **G.M. Whitesides**, (1998). Soft lithography, *Annual review of materials science, 28*, 153-184.

[3**] D. Psaltis**, **S.R. Quake, C. Yang,** (2006). Developing optofluidic technology through the fusion of microfluidics and optics, *Nature, 442,* 381-386.

[4] **J. Hübner**, **K.B. Mogensen, A.M. Jorgensen, P. Friis, P. Telleman, J.P. Kutter**, (2001). Integrated optical measurement system for fluorescence spectroscopy in microfluidic channels, *Review of Scientific Instruments, 72,* 229-233.

[5] **L. Mere**, T. Bennett, P. Coassin, P. England, B. Hamman, T. Rink, S. Zimmerman, P. Negulescu, (1999). Miniaturized FRET assays and microfluidics: key components for ultra-high-throughput screening, *Drug Discovery Today, 4*, 363-369.

[6] **K. Ramser**, **J. Enger, M. Goksör, D. Hanstorp, K. Logg, M. Käll**, (2005). A microfluidic system enabling Raman measurements of the oxygenation cycle in single optically trapped red blood cells, *Lab on a Chip, 5,* 431-436.

[7] **D. Cialla**, **A. März, R. Böhme, F. Theil, K. Weber, M. Schmitt, J. Popp,** (2012). Surface-enhanced Raman spectroscopy (SERS): progress and trends, *Analytical and bioanalytical chemistry, 403*, 27-54.

[8] **P.S. Dittrich**, **P. Schwille,** (2002). Spatial two-photon fluorescence cross-correlation spectroscopy for controlling molecular transport in microfluidic structures, *Analytical chemistry, 74*, 4472-4479.

[9] **X. Cheng**, **Y.-s. Liu, D. Irimia, U. Demirci, L. Yang, L. Zamir, W.R. Rodriguez, M. Toner, R. Bashir,** (2007). Cell detection and counting through cell lysate impedance spectroscopy in microfluidic devices, *Lab on a Chip, 7*, 746-755.

[10] **A.A.S. Bhagat, H. Bow, H.W. Hou, S.J. Tan, J. Han, C.T. Lim**, (2010). Microfluidics for cell separation, *Medical & biological engineering & computing, 48*, 999-1014.

[11] **D.R. Gossett**, **W.M. Weaver, A.J. Mach, S.C. Hur, H.T.K. Tse, W. Lee, H. Amini, D. Di Carlo,** (2010). Label-free cell separation and sorting in microfluidic systems, *Analytical and bioanalytical chemistry, 397*, 3249-3267.

[12] **A. Reece**, **B. Xia, Z. Jiang, B. Noren, R. McBride, J. Oakey,** (2016). Microfluidic techniques for high throughput single cell analysis, *Current opinion in biotechnology, 40*, 90-96.

[13] **H. Yin**, **D. Marshall,** (2012). Microfluidics for single cell analysis, *Current opinion in biotechnology, 23,* 110-119.

[14] **S. Dochow**, **C. Krafft, U. Neugebauer, T. Bocklitz, T. Henkel, G. Mayer, J. Albert, J. Popp,** (2011). Tumour cell identification by means of Raman spectroscopy in combination with optical traps and microfluidic environments, *Lab on a Chip, 11,* 1484-1490.

[15] **A.Y. Lau**, **L.P. Lee, J.W. Chan,** (2008). An integrated optofluidic platform for Raman-activated cell sorting, *Lab on a Chip, 8*, 1116-1120.

[16] **M. Li**, P.C. Ashok, K. Dholakia, W.E. Huang, (2012), Raman-activated cell counting for profiling carbon dioxide fixing microorganisms, *The Journal of Physical Chemistry A, 116*, 6560-6563.

[17] **F.C. Pascut**, **H.T. Goh, V. George, C. Denning, I. Notingher**, (2011). Toward label-free Raman-activated cell sorting of cardiomyocytes derived from human embryonic stem cells, *Journal of biomedical optics, 16:4,* 045002-045002-4.

[18] **Y. Song**, **H. Yin, W.E. Huang**, Raman activated cell sorting, (2016). *Current opinion in chemical biology, 33,* 1-8.

[19**] C.V. Raman, K.S. Krishnan,** (1928). A new type of secondary radiation, *Nature, 121*, 501-502.

[20] **J.H. Hibben**, **E. Teller,** (1939). Raman effect and its chemical applications, Retrieved from https://books.google.com.tr/books (Original work published in 1940)

[21] **D. Rank**, **J. McCartney**, (1948). Some spectral characteristics of mercury arcs for use in study of the Raman effect, *JOSA, 38,* 279-279.

[22] **F.H. Spedding**, **R.F. Stamm**, (1942). The Raman Spectra of the Sugars in the Solid State and in Solution I. The Raman Spectra of α-and β-d-Glucose, *The Journal of Chemical Physics, 10*, 176-183.

[23**] H. Welsh**, **M. Crawford, T. Thomas, G. Love**, (1952). Raman Spectroscopy of Low Pressure Gases and Vapors, *Canadian Journal of Physics, 30*, 577-596.

[24] **T. Gilson**, **PJ Hendra**, (1970). *Laser Raman Spectroscopy*, London, Wiley.

[25**] E. Lawson**, **B. Barry, A. Williams, H. Edwards**, (1997). Biomedical applications of Raman spectroscopy, *Journal of Raman Spectroscopy, 28,* 111-117.

[26] **L.P. Choo-Smith**, **H.G.M. Edwards, H.P. Endtz, J.M. Kros, F. Heule, H. Barr, J.S. Robinson, H.A. Bruining, G.J. Puppels,** (2002). Medical applications of Raman spectroscopy: From proof of principle to clinical implementation, *Biopolymers, 67,* 1-9.

[27] **P. Carey**, (2012). *Biochemical applications of Raman and resonance Raman spectroscopes*, Elsevier.

[28] **G. Başar**, **U. Parlatan, Ş. Şeninak, T. Günel, A. Benian, İ. Kalelioğlu**, (2012), Investigation of preeclampsia using raman spectroscopy, *Journal of Spectroscopy, 27,* 239-252.

[29] **U. Parlatan**, **G. Başar, N. Bavili, H. Yumru, F. Sag, S. Bulgurcuoglu, E. Bastu,** (2016). Embryo Viability Indexing Using Raman Spectroscopy of Spent Culture Media, *Spectroscopy Letters, 49:7*, 458-463.

[30] **J.C. Maxwell**, (1873*). A treatise on electricity and magnetism, Vol. II'*, Oxford, Clarendon Press.

[31] **E.F. Nichols**, **G. Hull**, (1901). A preliminary communication on the pressure of heat and light radiation, *Physical Review (Series I), 13*, 307.

[32] **P. Lebedev**, (1883). Experimental examination of light pressure, *Nuovo Cimento, 15,* 195.

[33] **E. Nichols**, **G. Hull**, (1903). The pressure due to radiation.(second paper.), *Physical Review (Series I), 17*, 26.

[34] **A. Ashkin**, (1970). Acceleration and trapping of particles by radiation pressure, *Physical review letters, 24*, 156.

[35] **A. Ashkin**, J**. Dziedzic, J. Bjorkholm, S. Chu**, (1986). Observation of a single-beam gradient force optical trap for dielectric particles, *Optics letters, 11,* 288-290.

[36] **K. Visscher**, **G. Brakenhoff, J. Krol**, (1993). Micromanipulation by "multiple" optical traps created by a single fast scanning trap integrated with the bilateral confocal scanning laser microscope, *Cytometry, 14*, 105-114.

[37] **K. Visscher**, **S.P. Gross, S.M. Block**, (1996). Construction of multiple-beam optical traps with nanometer-resolution position sensing, IEEE Journal of Selected *Topics in Quantum Electronics, 2*, 1066-1076.

[38] **D.L. Vossen**, **A. van der Horst, M. Dogterom, A. van Blaaderen,** (2004). Optical tweezers and confocal microscopy for simultaneous three-dimensional manipulation and imaging in concentrated colloidal dispersions, *Review of Scientific Instruments, 75*, 2960-2970.

[39] **E.R. Dufresne**, **D.G. Grier**, (1998). Optical tweezer arrays and optical substrates created with diffractive optics, *Review of scientific instruments, 69,* 1974-1977.

[40] **J. Liesener**, **M. Reicherter, T. Haist, H. Tiziani**, (2000). Multi-functional optical tweezers using computer-generated holograms, *Optics Communications, 185*, 77-82.

[41] **J.E. Curtis, B.A. Koss, D.G. Grier**, (2002). Dynamic holographic optical tweezers, *Optics Communications, 207*, 169-175.

[42] **G.C. Spalding, J. Courtial, R. Di Leonardo**, (2008).Holographic optical tweezers, *Academic Press*.

[43] **C. Creely**, **G. Volpe, G. Singh, M. Soler, D. Petrov**, (2005). Raman imaging of floating cells, *Optics express, 13,* 6105-6110.

[44] **C. Creely**, **S. Mercadal, G. Volpe, M. Soler, D. Petrov**, (2006). Raman imaging of neoplastic cells in suspension, SPIE Optics+ Photonics, *International Society for Optics and Photonics*, *6326*, 63260U.

[45] **K. Ramser**, **W. Wenseleers, S. Dewilde, S.V. Doorslaer, L. Moens**, (2008). The combination of resonance Raman spectroscopy, optical tweezers and microfluidic systems applied to the study of various heme-containing single cells, *Journal of Spectroscopy, 22*, 287-295.

[46] **J.R. Butler**, **J.B. Wills, L. Mitchem, D.R. Burnham, D. McGloin, J.P. Reid**, (2009). Spectroscopic characterisation and manipulation of arrays of sub-picolitre aerosol droplets, *Lab on a Chip, 9*, 521-528.

[47] **L. Kong**, **J. Chan**, (2014). A rapidly modulated multifocal detection scheme for parallel acquisition of Raman spectra from a 2-D focal array, Analytical chemistry, 86, 6604-6609.

[48] **Z. Pilát**, **J. Ježek, J. Kaňka, P. Zemánek**, (2014). Raman tweezers in microfluidic systems for analysis and sorting of living cells, *SPIE BiOS, International Society for Optics and Photonics*, pp. 89471M-89471M-89479.

[49] **H.D. Mallory**, (1950). On the Elimination of Extraneous Scattering in Raman Spectra, *The Journal of Chemical Physics, 18*, 898-898.

[50] **A. Molckovsky**, **L.-M.W.K. Song, M.G. Shim, N.E. Marcon, B.C. Wilson**, (2003). Diagnostic potential of near-infrared Raman spectroscopy in the colon: differentiating adenomatous from hyperplastic polyps, *Gastrointestinal endoscopy, 57*, 396-402.

[51] **D.I. Ellis**, **R. Goodacre**, (2006). Metabolic fingerprinting in disease diagnosis: biomedical applications of infrared and Raman spectroscopy*, Analyst, 131*, 875-885.

[52] **A.S. Haka**, **K.E. Shafer-Peltier, M. Fitzmaurice, J. Crowe, R.R. Dasari, M.S. Feld,** (2002). Identifying microcalcifications in benign and malignant breast lesions by probing differences in their chemical composition using Raman spectroscopy, *Cancer research, 62*, 5375-5380.

[53] **C. Krafft**, **G. Steiner, C. Beleites, R. Salzer**, (2009). Disease recognition by infrared and Raman spectroscopy, *Journal of biophotonics, 2*, 13-28.

[54] **N. Stone**, **P. Stavroulaki, C. Kendall, M. Birchall, H. Barr**, (2000). Raman spectroscopy for early detection of laryngeal malignancy: preliminary results, *The Laryngoscope, 110,* 1756-1763.

[55] **J.W. Chan**, **D.S. Taylor, T. Zwerdling, S.M. Lane, K. Ihara, T. Huser**, (2006). Micro-Raman spectroscopy detects individual neoplastic and normal hematopoietic cells*, Biophysical journal, 90*, 648-656.

[56] **W.F. Pearman**, **A.W. Fountain**, (2006). Classification of chemical and biological warfare agent simulants by surface-enhanced Raman spectroscopy and multivariate statistical techniques, *Applied spectroscopy, 60*, 356-365.

[57] **M. Shimoyama**, **H. Maeda, H. Sato, T. Ninomiya, Y. Ozaki**, (1997). Nondestructive discrimination of biological materials by near-infrared Fourier transform Raman spectroscopy and chemometrics: discrimination among hard and soft ivories of African elephants and mammoth tusks and prediction of specific gravity of the ivories, *Applied spectroscopy, 51*, 1154-1158.

[58] **C. Xie**, **J. Mace, M. Dinno, Y. Li, W. Tang, R. Newton, P. Gemperline**, (2005). Identification of single bacterial cells in aqueous solution using confocal laser tweezers Raman spectroscopy, *Analytical chemistry, 77*, 4390-4397.

[59] **K. Pearson, LIII**. (1901). On lines and planes of closest fit to systems of points in space, The London, *Edinburgh, and Dublin Philosophical Magazine and Journal of Science, 2*, 559-572.

[60] **H. Hotelling**, (1933). Analysis of a complex of statistical variables into principal components, *Journal of educational psychology, 24*, 417.

[61] **D.W. Hahn**, (2006). *Light scattering theory*, Department of Mechanical and Aerospace Engineering, Florida.

[62] **S. Hennani, L. Ez-zariy, A. Belafhal**, (2015). Radiation Forces on a Dielectric Sphere Produced by Finite Olver-Gaussian Beams, *Optics and Photonics Journal, 5*, 344.

[63] **D.J. Griffiths**, **R. College**, (1999). *Introduction to electrodynamics*, Upper Saddle River, NJ , Prentice Hall.

[64] **A. Ashkin**, (1992), Forces of a single-beam gradient laser trap on a dielectric sphere in the ray optics regime, *Biophysical journal, 61*, 569.

[65] **Url-1** *<http://www.tcichemicals.com/eshop/en/ca/category_index/12775/>*, data retrieved in 1.2.2017.

[66]. **J. Pros**t, (1995), *The physics of liquid crystals*, Oxford university press.

[67] **R.C. Jones**, (1941), A new calculus for the treatment of optical systems. description and discussion of the calculus, *JOSA, 31,* 488-493.

[68] **J. Neff**, **R. Athale, S.H. Lee**, (1990). Two-dimensional spatial light modulators: a tutorial, *Proceedings of the IEEE, 78*, 826-855.

[69] **Z. Kuang**, **D. Liu, W. Perrie, S. Edwardson, M. Sharp, E. Fearon, G. Dearden, K. Watkins,** (2009). Fast parallel diffractive multi-beam femtosecond laser surface micro-structuring, *Applied Surface Science, 255*, 6582-6588.

[70] **H. Zhang**, **J. Xie, J. Liu, Y. Wang,** (2009). Elimination of a zero-order beam induced by a pixelated spatial light modulator for holographic projection, *Applied optics, 48*, 5834-5841.

[71] **J.W. Goodman**, (2005). *Introduction to Fourier optics*, Roberts and Company Publishers.

[72] **M. Persson**, (2013). *Advances in Holographic Optical Trapping, (Ph.D. Thesis), Department of Physics*, University of Gothenburg, Gothenburg, Sweden.

[73] **R. Di Leonardo**, **F. Ianni, G. Ruocco**, (2007). Computer generation of optimal holograms for optical trap arrays, *Optics Express, 15*, 1913-1922.

[74] **R.W. Gerchberg**, (1972). A practical algorithm for the determination of phase from image and diffraction plane pictures, *Optik, 35*, 237.

[75] **M. Montes-Usategui, E. Pleguezuelos, J. Andilla, E. Martín-Badosa**, (2006), Fast generation of holographic optical tweezers by random mask encoding of Fourier components, *Optics express, 14*, 2101-2107.

[76**] M. Polin**, **K. Ladavac, S.-H. Lee, Y. Roichman, D. Grier**, (2005). Optimized holographic optical traps, *Optics Express, 13*, 5831-5845.

[77] **J.R. Ferraro**, (2003). *Introductory Raman Spectroscopy*, Academic press.

[78] **P.J. Hung**, **P.J. Lee, P. Sabounchi, R. Lin, L.P. Lee,** (2005). Continuous perfusion microfluidic cell culture array for high-throughput cell-based assays, *Biotechnology and bioengineering, 89*, 1-8.

[79] **A.E. Kamholz**, **B.H. Weigl, B.A. Finlayson, P. Yager,** (1999). Quantitative analysis of molecular interaction in a microfluidic channel: the T-sensor, *Analytical chemistry, 71*, 5340-5347.

[80] **W.G. Lee**, **Y.-G. Kim, B.G. Chung, U. Demirci, A. Khademhosseini,** (2010). Nano/Microfluidics for diagnosis of infectious diseases in developing countries, *Advanced drug delivery reviews, 62*, 449-457.

[81] **R.L. McCreery**, (2005). *Raman spectroscopy for chemical analysis*, John Wiley & Sons.

[82] **C.A. Lieber**, **A. Mahadevan-Jansen**, (2003). Automated method for subtraction of fluorescence from biological Raman spectra, *Applied spectroscopy, 57*, 1363-1367.

[83] **B. Başak**, et al., (2011).The Istanbul consensus workshop on embryo assessment: proceedings of an expert meeting, *Human reproduction (Oxford, England), 26*, 1270-1283.

[84] **D.K. Gardner**, **M. Lane,** (1993). Amino acids and ammonium regulate mouse embryo development in culture, *Biology of Reproduction, 48*, 377-385.

[85] **D.K. Gardner**, **M. Lane, P. Batt**, (1993). Uptake and metabolism of pyruvate and glucose by individual sheep preattachment embryos developed in vivo, *Molecular reproduction and development, 36*, 313-319.

[86**] B.D. Bavister**, **S.H. McKiernan**, (1993). Regulation of hamster embryo development in vitro by amino acids, *Preimplantation embryo development, Springer*, pp. 57-72.

[87] **H.M. Picton**, **K. Elder, F.D. Houghton, J.A. Hawkhead, A.J. Rutherford, J.E. Hogg, H.J. Leese, S.E. Harris,** (2010). Association between amino acid turnover and chromosome aneuploidy during human preimplantation embryo development in vitro, *Molecular human reproduction, 16*, 557-569.

[88] **R.L. Krisher**, **A.L. Heuberger, M. Paczkowski, J. Stevens, C. Pospisil, R.S. Prather, R.G. Sturmey, J.R. Herrick, W.B. Schoolcraft**, (2015). Applying metabolomic analyses to the practice of embryology: physiology, development and assisted reproductive technology, *Reproduction, fertility, and development*, *27:4*, 602-620.

[89] **C. Xie, Y.-q. Li,** (2003). Confocal micro-Raman spectroscopy of single biological cells using optical trapping and shifted excitation difference techniques, *Journal of Applied Physics, 93*, 2982-2986.

[90] **Url-2**, *< https://mathbits.com/MathBits/TISection/Statistics2/correlation.htm >*, in, 2016.

APPENDICES

APPENDIX A:

Computer program codes (In CD - Rom).

CURRICULUM VITAE

Name Surname   **:** Uğur PARLATAN

Place and Date of Birth   **:** ERZİNCAN, 30/08/1982

E-Mail   **:** **u.parlatan@gmail.com**

EDUCATION   **:**

- **B.Sc.**   **:** 2006, Yıldız Technical University, Science and Lectures Faculty, Physics Department

- **M.Sc.**   **:** 2010, Istanbul University, Science Faculty, Physics Department

PROFESSIONAL EXPERIENCE AND REWARDS:

- 2010 - 2011 Teaching Asistant at Işık University
- 2011 – 2017 Teaching Asistant at Istanbul University

PUBLICATIONS, PRESENTATIONS AND PATENTS ON THE THESIS:

- **U. Parlatan,** G. Başar, N. Bavili, H. Yumru, F. Sag, S. Bulgurcuoglu, E. Bastu, Embryo Viability Indexing Using Raman Spectroscopy of Spent Culture Media, Spectroscopy Letters, (2016).

- **Parlatan. U,** Bavili N., Oztürk T., Başar G.,Baştu E., Burgurcu Kuran S., Yumru H., Sağ F., "Embryo selection using Raman spectra of day three spent media", ICAVS 8, Wien, Austuria, 12-17 August 2015, pp 100-100.

- Bavili N**., Parlatan. U,** Başar G., **"**Construction of a Holographical Optical Tweezer set-up and Designing an interactive Graphical User Interface Program". IONS KARLSRUHE 2015.

- Demiral I., Bastu E., **Parlatan U.,** Bavili N., Yumru H., Bulgurcuoglu S., Basar G**.,** "Comparison of metabolomics profiling and morphological assessment for

evaluation of embryo quality and reproductive potential", ISGE 2016, GYNECOLOGICAL ENDOCRINOLOGY 32, 56-56.

OTHER PUBLICATIONS, PRESENTATIONS AND PATENTS:

- **Başar G., Parlatan U., Şeninak Ş., Günel T., Benian A., Kalelioğlu İ.,** "Investigation of Preeclampsia Using Raman Spectroscopy", Spectroscopy: An International Journal Volume 27, (2012), Issue 4, Pages 239-252.
- **Şeninak Ş., Parlatan U., Başar G., "**Band Component Analysis of Raman Spectra from Preeclamptic Serum and Plasma Samples**,** ECAMP 10, Salamanca, Spain, 4-9 July 2010.
- **Parlatan U., Şeninak Ş., Başar G., "**Investigation of Preeclampsia by Analysing the Raman Spectra from Serum and Plasma Samples : A Chemometrics Approach**,** ECAMP 10, Salamanca, Spain, 4-9 July 2010.
- **Başar G., Parlatan U., Şeninak Ş., "**Investigation Of Preeclampsia By Raman Spectroscopy**,** ICORS 10, Massachusetts, Boston, 8-13 August 2010.
- **Başar Gö, Başar Gü., Parlatan U., Şeninak Ş., "**Interaction Of Kyotorphin In Different Concentrations With The Membrane Of Optically Trapped DMPC Vesicle**,** ICORS 10, Massachusetts, Boston, 8-13 August 2010.
- **Başar G., Parlatan U., Şeninak Ş., Günel T., Benian A., Kalelioğlu İ, "**Preeklampsi Hastalığının Raman Spektroskopi Yöntemi ile İncelenmesi**, TFD 27** Istanbul, Türkiye, 4-17 Eylül 2010.
- **Şeninak Ş., Parlatan U., Inci F., Kok F. N., Basar G.,** "Investigation of Modifications in Physiochemical Structure of Liposomes Due to Transmembrane Proteins by Raman Tweezers", TFD 28, Türkiye, 6-8 September 2011.
- **Parlatan U., Şeninak Ş., Inci F., Kok F. N., Basar G.,** "Investigation of Effects of Transmembrane Proteins Presence on Liposomes by Raman Tweezers", TFD 28, Türkiye, 6-8 September 2011.